AFRL-RV-PS-
TR-2021-0037

STATE INITIALIZATION USING DOPPLER-SHIFT OF RADIO FREQUENCY SIGNALS

John A. Christian and Christopher Ertl

Rensselaer Polytechnic Institute
110 8th Street
Troy, NY 12180

15 May 2021

Final Report

AIR FORCE RESEARCH LABORATORY
Space Vehicles Directorate
3550 Aberdeen Ave SE
AIR FORCE MATERIEL COMMAND
KIRTLAND AIR FORCE BASE, NM 87117-5776

NOTICE AND SIGNATURE PAGE

Using Government drawings, specifications, or other data included in this document for any purpose other than Government procurement does not in any way obligate the U.S. Government. The fact that the Government formulated or supplied the drawings, specifications, or other data does not license the holder or any other person or corporation; or convey any rights or permission to manufacture, use, or sell any patented invention that may relate to them.

This report is the result of contracted fundamental research which is exempt from public affairs security and policy review in accordance with AFI 61-201, paragraph 2.3.5.1. This report is available to the general public, including foreign nationals. Copies may be obtained from the Defense Technical Information Center (DTIC) (http://www.dtic.mil).

AFRL-RV-PS-TR-2021-0037 HAS BEEN REVIEWED AND IS APPROVED FOR PUBLICATION IN ACCORDANCE WITH ASSIGNED DISTRIBUTION STATEMENT.

//signed//

THOMAS LOVELL
Program Manager

//signed//

ANDREW SINCLAIR
Tech Advisor, Space Component
Technology Branch

//signed//

JOHN BEAUCHEMIN
Chief Engineer, Spacecraft Technology Division
Space Vehicles Directorate

This report is published in the interest of scientific and technical information exchange, and its publication does not constitute the Government's approval or disapproval of its ideas or findings.

Approved for public release; distribution is unlimited.

REPORT DOCUMENTATION PAGE

Form Approved
OMB No. 0704-0188

1. REPORT DATE *(DD-MM-YYYY)*	2. REPORT TYPE	3. DATES COVERED *(From - To)*
15-05-2021	Final Report	25-Jul-2019 - 15-May-2021

4. TITLE AND SUBTITLE

State Initialization using Doppler-Shift of Radio Frequency Signals

5a. CONTRACT NUMBER
FA9453-19-1-0013

5b. GRANT NUMBER

5c. PROGRAM ELEMENT NUMBER
61102F

6. AUTHOR(S)

John A. Christian and Christopher Ertl

5d. PROJECT NUMBER
3001

5e. TASK NUMBER
EF133182

5f. WORK UNIT NUMBER
V1FH

7. PERFORMING ORGANIZATION NAME(S) AND ADDRESS(ES)

Rensselaer Polytechnic Institute
110 8th Street
Troy, NY 12180

8. PERFORMING ORGANIZATION REPORT NUMBER

9. SPONSORING / MONITORING AGENCY NAME(S) AND ADDRESS(ES)

Air Force Research Laboratory
Space Vehicles Directorate
3550 Aberdeen Ave SE
Kirtland AFB, NM 87117-5776

10. SPONSOR/MONITOR'S ACRONYM(S)
AFRL/RVSV

11. SPONSOR/MONITOR'S REPORT NUMBER(S)
AFRL-RV-PS-TR-2021-0037

12. DISTRIBUTION / AVAILABILITY STATEMENT
Approved for public release; distribution is unlimited.

13. SUPPLEMENTARY NOTES
State Initialization using Doppler-Shift of Radio Frequency Signals

14. ABSTRACT

This work investigates a number of techniques for estimating the position and velocity of an unknown radio frequency (RF) transmitter. A number of RF observables are considered, including direction of arrival, time difference of arrival, and Doppler shift. Mathematical models are developed for each of these observable types. A root locus technique is developed for localization of a transmitter fixed to the surface of Earth (the so-called geolocation problem). Preliminary analysis and techniques are presented for the localization of an unknown orbiting transmitter.

15. SUBJECT TERMS
Orbit Determination, Radio Frequency (RF) Transmitter Localization

16. SECURITY CLASSIFICATION OF:			17. LIMITATION OF ABSTRACT	18. NUMBER OF PAGES	19a. NAME OF RESPONSIBLE PERSON
a. REPORT	b. ABSTRACT	c. THIS PAGE			Thomas Lovell
Unclassified	Unclassified	Unclassified	Unlimited	58	19b. TELEPHONE NUMBER *(include area code)*

--- This Page Intentionally Left Blank ---

TABLE OF CONTENTS

Page

LIST OF FIGURES

Page

LIST OF TABLES

Page

--- This Page Intentionally Left Blank ---

1 SUMMARY

This report describes the work completed under grant FA9453-19-1-0013 entitled “State Initialization using Doppler-Shift of Radio Frequency Signals.” During the grant period of performance, the research team at Rensselaer Polytechnic Institute (RPI) investigated how signals from an unknown radio frequency (RF) transmitter might be used to infer the state (position and velocity) of the unknown transmitter. The work began by looking at Doppler observables, but quickly expanded to include a full array of RF observables --- including direction of arrival (DOA), time difference of arrival (TDOA), and others. We demonstrated how these observables might be used for geolocation (finding the position of a stationary transmitter on the Earth’s surface), initial orbit determination (IOD), and sequential estimation in an extended Kalman filter (EKF). Theoretical analyses and numerical studies were performed to determine the efficacy of different RF observables in different scenarios. Our work to date demonstrates that RF observables may be used to localize a transmitter, though additional investigation is required to arrive at numerically stable solutions for the fully generic state initialization (e.g., initial orbit determination) problem.

2 INTRODUCTION

Navigation is vital for any vehicle requiring knowledge of its position and velocity to achieve its mission. Much of modern navigation is done using radio-frequency (RF) measurements, with applications across nearly all application environments --- land, maritime, air, and space. Examples of RF-based navigation systems abound, such as trilateration-based systems (e.g., Global Positioning System (GPS)) and hyperbolic positioning systems (e.g., Loran-C) [1]. The proposed work explores the mathematics of RF-only localization. The exact same mathematical framework may be used to (1) localize an unknown transmitter with signals received at many stations or (2) to navigate a vehicle whose receiver observes signals originating from many known transmitters.

Widespread use of Doppler measurements for vehicle localization dates back to World War II, and Doppler measurements have remained a valuable tool in navigation since then. Doppler measurements are easily attainable, and sources of waves from which to take these measurements are pervasive and inexpensive. Doppler navigation can be done using RF measurements taken from WiFi sources [2] [3], from TV and cell phone towers [4] [5], from GPS satellites [6] [7], and from many other sources.

In this work, we focus on the problem of localizing a RF transmitter broadcasting at an unknown frequency from an unknown location. The simplest scenario is the geolocation problem, where the transmitter is assumed to be stationary on the surface of the Earth---and we develop a number of solutions for this specific situation. More challenging is the case of a moving transmitter, which would generally be the case for a transmitting satellite. In this situation, both the position and velocity of the transmitter are unknown. Relatively straightforward solutions exist when concurrent observations are available, and the problem becomes more complicated for non-concurrent measurements.

3 METHODS, ASSUMPTIONS, AND PROCEDURES

Radiometric navigation uses the principles of RF wave propagation to infer information about a vehicle's state—which, in our case, is the unknown transmitter's location and (in some cases) velocity. RF signals produce at least three fundamental classes of measurements: bearing-based [8] [9], time-based [10] [11], and Doppler-based [12] [13]. Here, we develop models for all three measurement types.

First, we develop the background necessary to obtain bearing measurements from observed RF signals. We choose to focus on the well-known MUSIC algorithm, though other options do exist.

Second, we develop time-based and frequency-based measurements. TDOA and FDOA techniques are commonly used in the application of geolocation. One common time-based technique, TDOA, uses the difference in the time of arrival of one signal measured by two receivers [14]. Similar to TDOA, we will focus on the FDOA technique that differences the measured frequency by two receivers [15]. There are techniques that involve both TDOA and FDOA measurements [16] [17].

Finally, we briefly explore the efficacy of MUSIC-based orbit determination within the context of an extended Kalman filter (EKF).

3.1 RF-Based Bearing Measurements: The MUSIC Algorithm

The MUltiple SIgnal Classification (MUSIC) algorithm is used to estimate Direction-Of-Arrival (DOA) of multiple received signals [18]. The algorithm requires a uniform linear array (ULA) of radio receivers with m number of elements, where m is greater than the number of uncorrelated signals [19], k. Of particular note, numerous authors have investigated the efficacy of the MUSIC algorithm for estimating the DOA of interference signals [20] [21]. These example works both consider the problem of finding transmitters attempting to interfere with GNSS signals. The article [20] provides two antenna arrays recommendations and the results for both.

The array samples the signals and produces an observation vector $\boldsymbol{y}(t)$ with an m number of elements. A 2-d diagram of this can be seen in Figure 1, where each black box is an element of the ULA, d is the distance between each element, and θ is the angle at which the signal arrives at each element.

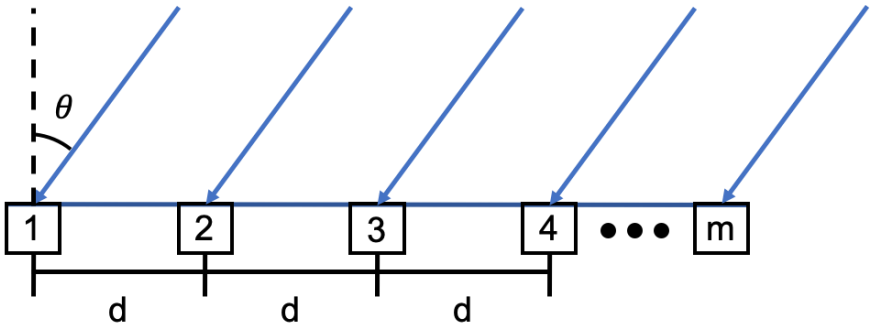

Figure 1. A simple diagram of a Uniform Linear Array

This vector encompasses the signal sample from each element of the array at that time step. This observational vector, also called a snapshot, can be modeled as a linear combination of k incident signals and additive Gaussian noise using the equation,

$$\boldsymbol{y}(t) = A\boldsymbol{s}(t) + \boldsymbol{\omega} \tag{1}$$

where A is an $m \times k$ steering vector matrix, $\boldsymbol{s}(t)$ is a $k \times 1$ vector that encompasses the incident signals' amplitude and phase, and $\boldsymbol{\omega}$ is an $m \times 1$ Gaussian noise vector. Each column of the steering vector matrix is made up of the incident signal mode vectors, or steering vectors. These steering vectors, denoted as $\boldsymbol{\beta}(\theta)$ are functions of the signal's angle of arrival and the distance between each element of the ULA. To determine the DOA we will need to extract the angle of arrival from the steering vectors. We can do this by exploiting the fact that the steering vectors for the angle of each incident signal span the signal subspace which is disjoint from the noise subspace.

The goal of the MUSIC algorithm is to determine the DOA of each incident angle measured by the array. This is accomplished by determining the incident signal subspace and the noise subspace using through eigenvalue decomposition. We begin by estimating the covariance matrix from multiple snapshots taken by the array. This is primarily done through time averaging using the equation,

$$R = \frac{1}{N}\sum_{i=1}^{N} \boldsymbol{y}(t_i)\boldsymbol{y}(t_i)^H \tag{2}$$

where N is the number of snapshots used to estimate the covariance matrix and H is the Hermitian conjugate. We can also express the signal covariance matrix as

$$R = E[\boldsymbol{y}\boldsymbol{y}^H] \tag{3}$$

After some manipulation, we can express the covariance matrix as

$$R = AE[\boldsymbol{s}\boldsymbol{s}^H]A^H + E[\boldsymbol{\omega}\boldsymbol{\omega}^H] = AR_sA^H + R_\omega \tag{4}$$

where R_s is the incident signal covariance matrix and R_ω is the noise covariance matrix. An eigenvalue decomposition is performed on the covariance matrix we estimated, R. From this eigenvalue decomposition, an $n = m - k$ number of eigenvalues on the order of the noise variance are chosen as noise eigenvalues. The eigenvectors related to these eigenvalues span the noise subspace and make up the matrix Q_ω. Using the known steering vector function of the array, $\boldsymbol{\beta}(\theta)$, we can sweep a range of angles to estimate the power at each angle using the equation

$$P = \frac{1}{\boldsymbol{\beta}^H(\theta)Q_\omega Q_\omega^H \boldsymbol{\beta}(\theta)} \tag{5}$$

The peaks of the power spectrum provide the DOA of each incident signal received by the array [18] [22].

MUSIC is limited by the need for all signals to be non-coherent [19] [21] and is affected by the signal-to-noise ratio (SNR) [21], spacing between each element in the array [22] and the number of elements in the array [23] [22]. These effects can be limited with a higher SNR, setting the distance between the elements to half the expected signal wavelength [22], and increasing the number of elements in the array [23] [22].

Accuracy of the MUSIC algorithm is affected by a multitude of parameters including the parameters mentioned in the previous paragraph. Depending on the hardware and scenario the accuracy for MUSIC can ranges from about 0.001 degrees [19] to about 10 degrees [21]. Two variations of the MUSIC algorithm that improves upon the accuracy include the Root-MUSIC algorithm [19] [24] and the STC-MUSIC [21]. Root-MUSIC couches the problem as a polynomial and solves for its roots to estimate the DOA while STC-MUSIC introduces a focusing parameter. Another MUSIC variation actually suppresses all other signals than the target's [25]. For this algorithm to work, an approximation of the target's bearing must be known *a priori*.

There are a variety of alternatives to the classical MUSIC algorithm, such as those presented in [26] and [27]. A full comparative assessment of RF-based DOA algorithms within the context of space transmitter localization is a topic of future work. We focus just on MUSIC here.

3.2 RF-Based Timing Measurements: TDOA

Time-based measurements use the time it takes for the signal to travel between two points to estimate the distance between the two points. For TDOA we will take the difference in time measurements at two different receiver locations.

We begin our derivation of TDOA by considering the time required for the RF signal to travel from the unknown transmitter to one of the known receivers. Assuming light travels at a constant speed c (taken to be the speed of light in a vacuum), one may compute the so-called pseudo-range as

$$\rho_i = c\left[t_{r_i} - t_T\right] \tag{6}$$

where t_{r_i} is the time the signal was observed by the i-th receiver and t_T is the (unknown) time of signal transmission. The distance ρ_i is called the pseudo-range since it varies from the true geometric range due to receiver clock errors and changes in the speed of light as it passes through various media between the transmitter and receiver.

In the TDOA problem, we are concerned with the difference between when the signal arrives at the i-th receiver (t_{r_i}) and the j-th receiver (t_{r_j}). This equates to a pseudo-range difference

$$\Delta\rho = \rho_j - \rho_i = c\left[t_{r_j} - t_T\right] - c\left[t_{r_i} - t_T\right] = c\left[t_{r_j} - t_{r_i}\right] \tag{7}$$

3.2.1 Clock Bias

The clock bias of the receivers cause measured time to be different from the true time. We can see this in the receiver time equation

$$t_r(t) = t + \delta t_r(t) \tag{8}$$

where t is the true time and $\delta t(t)$ is the clock bias for the receiver at time t. If the receivers were to be synchronized with a GPS clock, the biases for both clocks would be on the order of $\sim 10^{-9}$ seconds [28]. Combining Eqs. 6 and 8 we find the difference between the transmit and measured receiver time to obtain the pseudo-range

$$\begin{aligned} \rho_i &= c\left[t_{r_i}(t_T + \tau_i) - t_T\right] \\ &= c\left[t_T + \tau_i + \delta_{r_i}(t_T + \tau_i) - t_T\right] \\ &= c\left[\tau_i + \delta t_{r_i}(t_T + \tau_i)\right] \\ &= c\tau_i + c\delta t_{r_i}(t_T + \tau_i) \end{aligned} \tag{9}$$

where ρ is the pseudo-range along the line of sight between the transmitter and receiver and τ is the time elapsed between transmission and receiving. With the atmospheric delays, we now know that the measured range from the time of flight from the signal is

$$c\tau_i = \left\| \boldsymbol{r}_{r\_i/T}(t_T + \tau_i) \right\| + I_{\rho_i} + TR_{\rho_i} \tag{10}$$

where $\boldsymbol{r}_{r\_i/T}(t_T + \tau_i)$ is the magnitude of the distance from receiver to transmitter, I_ρ is the ionosphere delay, and TR_ρ is the troposphere path delay. Combining Eqs. 9 and 10 we can see that the pseudo-range is the summation of the distance between the receiver and transmitter, clock bias, ionosphere path delay, and the troposphere path delay.

3.2.2 Tropospheric Path Delay

As the signal travels between the transmitter and the receiver the signal is delayed by the different media it must propagate through. This delay derives from the media changing the speed at which light propagates through them. In our scenario, the two largest delays come from the troposphere and ionosphere. From basic optics, the index of refraction

$$n = c/c_m \tag{11}$$

is the ratio of the speed of light in a vacuum and the speed of light in the medium, c_m. To find the excess delay let us begin with the first principles equation

$$c_m(l) = \frac{dl}{dt} \tag{12}$$

where the speed of light in the medium is the time derivative of the position of the signal along the signal path, l. Through some minor manipulation we can find the time it takes the signal to travel through the medium

$$\tau = \frac{1}{c}\int_T^R \frac{c}{c_m(l)}\, dl = \frac{1}{c}\int_T^R n(l)\, dl \tag{13}$$

where we integrate along the signal path from the transmitter, T, and receiver, R. To find the excess time delay we can set $c_m = c$ and find

$$\tau_0 = \frac{1}{c}\int_T^R \frac{c}{c} dl = \frac{1}{c}\int_T^R dl \tag{14}$$

where τ_0 is the time it takes the signal to travel from the transmitter to the receiver in a vacuum. Subtracting Eq. 13 from Eq. 14 we find the excess time delay equation to be

$$\Delta\tau = \tau - \tau_0 = \frac{1}{c}\int_T^R [n(l) - 1]\, dl \tag{15}$$

The initial medium the signal propagates through is the troposphere. The troposphere spans from the earth's surface to an average height of about 12 km. The troposphere contains a majority of the Earth's gasses and water vapor which are the two main sources of delay. To derive our tropospheric delay, we begin by defining refractivity [28] as $N = (n - 1) \times 106$. The refractivity of the troposphere can be split into the refractivity of the dry gasses and the water vapors

$$N = N_d + N_w \tag{16}$$

where N_d is the dry refractivity and N_w is the wet refractivity. The refractivity for dry and wet are well-modeled as [28]

$$\begin{aligned} N_d &= 77.64\frac{P}{T} \\ N_w &= 3.73 \times 10^5 \frac{e}{T^2} \end{aligned} \tag{17}$$

where e is the partial pressure from the water vapors and P is the total pressure with both measured in millibars and T is the temperature in kelvin. We can find the excess measured distance (the excess time delay multiplied by the speed of light) by combining Eqs. 15 and 17

$$TR_{\rho z} = 10^{-6} \int [N_d(l) + N_w(l)]\, dl \tag{18}$$

where $TR_{\rho z}$ is the zenith tropospheric delay (meters). There are multiple models to measure tropospheric delay including the Saastamoinen model [29] and the Hopfield model [30].

The zenith tropospheric delay must be scaled with respect to the elevation angle of the receiving satellite compared to the transmitter. This is because at lower elevation angles there is a longer path taken through the troposphere causing an excess delay to the zenith delay. This scaling is achieved by multiplying the zenith tropospheric delay by an obliquity factor. Most simple models use the same obliquity factor for the wet and dry delay [28]

$$OF_{TR}(el) = \frac{1}{\{1 - [\cos(el)/1.001]^2\}^{-1/2}} \tag{19}$$

where $OF_{TR}(el)$ is the obliquity factor for the tropospheric delay in terms of elevation angle. Combining Eqs. 18 and 19 the tropospheric delay is

$$TR_\rho = TR_{\rho z} OF_{TR}(el) \tag{20}$$

3.2.3 Ionospheric Path Delay

After the troposphere, the signal then propagates through the ionosphere. The Earth's ionosphere is an ionized region spanning from about 60-1,000 km above the Earth's surface. The main sources of the ions come from photoionization (high energy photons are absorbed by particles leading to ionization) and energetic particle collisions [31]. The total electron content (TEC) in the path of the signal is the major contributor to ionospheric delay [28] and is measured using the equation

$$TEC = \int_T^R \eta_e(l)\, dl \tag{21}$$

where η_e is the electron density along the path of the signal. The index of refraction of the ionosphere [28] for RF signals is

$$\eta_I = 1 + \frac{40.3\eta_e}{f^2} \tag{22}$$

where f is the frequency of the signal. We can see from this equation that the index of refraction is based on the signal's frequency making the ionosphere a dispersive medium. Combining Eqs. 21, 22, and 15 we find the equation for excess measured distance from the ionosphere is

$$I_{\rho z} = 40.3\frac{TEC}{f^2} \tag{23}$$

where $I_{\rho z}$ is the zenith ionospheric delay (meters). The most widely used model to solve for the ionospheric delay is the Klobuchar model [32].

Similar to the tropospheric delay, the zenith ionospheric delay must be scaled using an obliquity factor. A common model used for the obliquity factor for ionospheric delay makes the assumption that the ionosphere is a thin shell around the Earth and is pierced at a height of h_I [28]. Instead of using the elevation angle, we use its complement, or zenith angle (ζ) when defining the obliquity factor as [28]

$$OF_I(\zeta) = 1 - \left[\frac{R_E \sin(\zeta)}{R_E + h_I}\right]^2 \tag{24}$$

where $OF_I(\zeta)$ is the obliquity factor of the ionospheric delay in terms of zenith angle, R_E is the radius of the Earth, and h_I is the height of the ionosphere thin shell above the Earth's surface. Combining Eqs. 23 and 24 the ionospheric delay is

$$I_\rho = I_{\rho z} OF_I(\zeta) \tag{25}$$

3.2.4 TDOA Equation

Combining Eqs. 9 and 10 we get the full pseudo-range equation

$$\rho_i(t_T + \tau_i) = \left\|\boldsymbol{r}_{r_{i/T}}(t_T + \tau_i)\right\| + c\left[\delta t_{r_i}(t_T + \tau_i)\right] + I_{\rho_i} + TR_{\rho_i} \tag{26}$$

Since TDOA is the difference in time measurements by the two receivers, multiplying the measurements by the speed of light will yield the difference in pseudo-ranges. Using Eq. 7 we get the TDOA equation

$$\begin{aligned} c(\tau_j - \tau_i) &= \rho_j - \rho_i = \Delta\rho \\ &= \left\|\boldsymbol{r}_{r_{j/T}}(t_T + \tau_j)\right\| - \left\|\boldsymbol{r}_{r\_i/T}(t_T + \tau_i)\right\| + c\left[\delta t_{r_j}(t_T + \tau_i)\right] - c\left[\delta t_{r_i}(t_T + \tau_i)\right] + I_{\rho_j} - I_{\rho_i} \\ &\quad + TR_{\rho_j} - TR_{\rho_i} \end{aligned} \tag{27}$$

Table 1 provides the order of magnitude for each error source for TDOA. This includes error from models or in the case of clock synchronization error, synchronizing clocks with GPS satellites. The clock bias delay without synchronization depends on each receiver's clock offset and clock drift. Knowing both the offset and drift, the clock bias can be solved for. The order of magnitude for tropospheric and ionospheric delay [28] are provided with and without models. Since these are constantly changing and every new TDOA measurement comes with a new pair of ionosphere and troposphere terms, including them as solve for terms would add unknowns faster than new equations. It is not evident how one would solve for $I_{\rho j} - I_{\rho i}$ and $TR_{\rho j} - TR_{\rho i}$ within the TDOA-based geolocation problem. Thus, ionosphere and troposphere delay terms and errors in their associated models place a performance floor on TDOA-based geolocation, regardless of the sensor system being used.

Table 1: Order of magnitude of each error source for TDOA

Error Sources	Delay w/o Model(s)	Delay w/ Model(s)	Can be Solved For?
Clock Synchronization Error	Depends on clocks	10^{-9}	Y
Tropospheric Delay	10^{-9}	10^{-10}	N
Ionospheric Delay	10^{-8}	10^{-9}	N

In some cases, it may be necessary to solve for the bias between the two receiver clocks. For simplicity, let us define clock offset as

$$U = c[\delta t_{r_j}(t_T + \tau_j) - \delta t_{r_i}(t_T + \tau_i) \tag{28}$$

and the vector from transmitter to receiver is

$$\left\|\boldsymbol{r}_{r_{i/T}}\right\| = \left\|\boldsymbol{r}_{r_i} - \boldsymbol{r}_T\right\| \tag{29}$$

Using basic algebra, we expand Eq. 27 to a polynomial in terms of (x_T,y_T,z_T,U) where (x_T,y_T,z_T) are the cartesian components of the transmitter's location, (x_i,y_i,z_i) are the Cartesian components of the i^{th} orbiting receiver positions, and we define $K_i = x_i^2 + y_i^2 + z_i^2$. Note that

this is a fourth order polynomial in terms of four variables. Thus, we may solve for the transmitter's location if we take four TDOA measurements. According to Bèzout's theorem, such a polynomial will yield at most 256 unique solutions. If U was set to zero the polynomial would match the geometric only simultaneous TDOA polynomial [33]. Using the Bèzout's theorem we can see such a polynomial will yield at most 8 solutions.

In order to preliminarily assess our polynomial's response to measurement and clock synchronization error, we perform a Monte Carlo simulation on the geometric only simultaneous TDOA polynomial in which we include the TDOA measurement errors detailed in Table 1. The atmospheric error includes the tropospheric and ionospheric delay which is changing for all three measurements. The clock synchronization error is kept constant for all three measurements. In performing the Monte Carlo trials, the clock error and atmospheric error are considered Gaussian. The range of sigma levels considered for these errors are indicated on the x and y axes of Figure 2. For each trial, three TDOA measurements were simulated, the three second-order polynomials were solved, and the position error magnitude between the true transmitter location and the solution closest to this location was calculated. The scenario chosen for this Monte Carlo simulation includes two receiver satellites in a leader-follower formation in a low Earth orbit. The transmitter's position on Earth is 35° north and 92° east. Figure 2 shows us that the position error magnitude is more sensitive to the atmospheric error than the clock synchronization error.

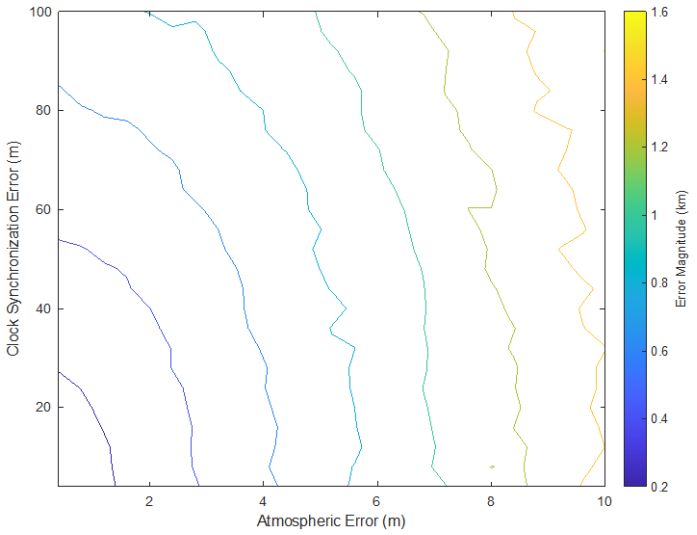

Figure 2. Monte Carlo simulation results

3.3 RF-Based Frequency Measurements: FDOA and FROA

In this section, we will focus on the Doppler-based measurements involved in localization. Doppler-based measurements use Doppler shift to estimate the component of the relative velocity along the line-of-sight direction, or range-rate. For FDOA and FROA using the range rate difference, or ratio, of two satellites allows us to estimate the position of the transmitter.

Let us begin our derivation of both equations by first defining frequency shift as

$$z = \frac{f - f_T}{f_T} = \frac{\Delta f}{f_T} \tag{30}$$

where f is the shifted frequency and f_T is the original (transmitted) frequency. As a signal propagates from the Earth's surface to an orbiting receiver

$$\begin{aligned} f_m &= \frac{f_m}{f_D}\frac{f_D}{f_I}\frac{f_I}{f_{TR}}\frac{f_{TR}}{f_T} f_T \\ &= [z_m + 1\,][z_D + 1][z_I + 1\,][z_{TR} + 1] f_T \end{aligned} \tag{31}$$

where f_m is the frequency measured by the receiver, z_m is the measurement frequency shift, z_D is the relativistic Doppler shift, z_I is the ionospheric frequency shift, and z_{TR} is the tropospheric frequency shift.

3.3.1 Measurement Frequency Shift

We will begin by looking at the frequency shift from measurement error. These measurement errors come from receiver instrumental noise [34] and can be modeled as a frequency shift with the equation

$$\begin{aligned} f_m &= f_0 + f_0 f_{ai} \\ &= f_0[1 + f_{ai}] \end{aligned} \tag{32}$$

where f_0 is the original frequency received and f_{ai} is the accuracy of the frequency measured by the receiver. This leads to the equation

$$z_{mi} + 1 = \; 1 + f_{ai} \tag{33}$$

3.3.2 Relativistic Doppler Shift

The next frequency shift is the relativistic Doppler shift. The frequency of a signal is shifted due to the relative velocity between the receiver and the transmitter. Let us first define for simplicity

$$\boldsymbol{\beta}_i = \frac{\boldsymbol{v}_{r_i/T}}{c} \tag{34}$$

where $\boldsymbol{v}_{r_i/T}$ is the relative velocity between the receiver and transmitter. The Lorentz transformation [35], used in Special Relativity as a transformation from a stationary frame to a moving frame, is then defined to be

$$\gamma = \frac{1}{\sqrt{1 - \boldsymbol{\beta}_i^T \boldsymbol{\beta}_i}} \tag{35}$$

The relativistic Doppler shift as defined by Einstein's 1905 paper on the Theory of Special Relativity is defined as [35]

$$f_D = \frac{f_0}{\gamma[1 - \boldsymbol{\beta}_i^T \boldsymbol{u}_i]} \tag{36}$$

where f_D is the frequency observed in the moving frame and $\boldsymbol{u}_i$ is the unit vector pointing from the spacecraft to the transmitter. This vector can be expressed as,

$$\boldsymbol{u}_i = \frac{\boldsymbol{r}_{T/r_i}}{\left\| \boldsymbol{r}_{T/r_i} \right\|} \tag{37}$$

Since $\|\boldsymbol{\beta}_i\|$ is on the order of 10^{-6} in our scenario, we can perform a Taylor Series expansion on Eq. 36 about $\boldsymbol{\beta}_i = \mathbf{0}_{3\times1}$. This gives us the equations [36]

$$\gamma^{-1} = 1 - \frac{\boldsymbol{\beta}_i^T \boldsymbol{\beta}_i}{2} + \mathcal{O}(\boldsymbol{\beta}^4) \tag{38}$$

and

$$[1 - \boldsymbol{\beta}_i^T \boldsymbol{u}_i]^{-1} = 1 + \boldsymbol{\beta}_i^T \boldsymbol{u}_i + [\boldsymbol{\beta}_i^T \boldsymbol{u}_i]^2 + [\boldsymbol{\beta}_i^T \boldsymbol{u}_i]^3 + \mathcal{O}(\boldsymbol{\beta}^4) \tag{39}$$

where $\mathcal{O}(\boldsymbol{\beta}^4)$ are the fourth order terms. Combining Eqs. 38 and 39 we get

$$z_D + 1 = 1 + \boldsymbol{\beta}_i^T \boldsymbol{u}_i + \left\{ [\boldsymbol{\beta}_i^T \boldsymbol{u}_i]^2 - \frac{\boldsymbol{\beta}_i^T \boldsymbol{\beta}_i}{2} \right\} + \left\{ [\boldsymbol{\beta}_i^T \boldsymbol{u}_i]^3 - \frac{\boldsymbol{\beta}_i^T \boldsymbol{\beta}_i \boldsymbol{\beta}_i^T \boldsymbol{u}_i}{2} \right\} + \mathcal{O}(\boldsymbol{\beta}^4) \tag{40}$$

In our scenario, the relativistic Doppler shift comes from the relative velocity between a ground based transmitter and an orbiting receiver. Suppose the receiver is in a circular orbit 200 kilometers above the Earth's surface. The relative velocity between the orbiting receiver and the stationary transmitter will be around $7.79 \frac{km}{s}$ .This means the second order terms of $\boldsymbol{\beta}_i$ is on the order of 10^{-10}. With this knowledge, we have decided to simplify the equation to only include the linear term

$$z_{D_i} + 1 = 1 + \boldsymbol{\beta}_i^T \boldsymbol{u}_i \tag{41}$$

3.3.3 Ionospheric Frequency Shift

As discussed before, as RF signals propagate through the Earth's atmosphere there is a delay to the signal due to the medium's index of refraction. This causes a phase advance to the signal

[28]. The change in refraction of the medium causes a change in phase advance and in turn a shift in frequency. This is because instantaneous frequency is defined as

$$f(t) = \frac{d\theta(t)}{dt} \tag{42}$$

where $\theta(t)$ is the instantaneous phase. Therefore, our ionospheric effect on frequency is the time derivative of the effect on phase [37]

$$I_{fi}(t) = \frac{40.3}{cf_0}\frac{dTEC}{dt} \tag{43}$$

where f_0 is the frequency before the effect. The ionospheric shift on frequency is

$$z_{I_i} + 1 = 1 + I_{fi} \tag{44}$$

Unfortunately, the authors were unable to find any models for the time derivative of TEC in the ionosphere.

3.3.4 Tropospheric Frequency Shift

Similar to the ionospheric frequency shift, the temporal change in the troposphere's index of refraction causes a shift in frequency. The tropospheric effect is defined as [38]

$$TR_{fi}(t) = -10^{-6}\frac{f_0}{c}\int \frac{dN_d(l,t)}{dt} + \frac{dN_w(l,t)}{dt}dl \tag{45}$$

The tropospheric frequency shift is

$$z_{TR_i} + 1 = 1 + TR_{fi} \tag{46}$$

Similar to Ionospheric frequency shift, the authors were unable to find any models for the changes in refractivity of the troposphere.

3.3.5 FDOA Equation

With the four frequency shifts accounted for, we can substitute Eqs. 33, 41, 44, and 46 into Eq. 31 to get

$$\begin{aligned}\frac{f_m}{f_T} &= \left[z_{m_i} + 1\right]\left[z_{D_i} + 1\right]\left[z_{TR_i} + 1\right] \\ &= 1 + \boldsymbol{\beta}_i^T\boldsymbol{u}_i + [1 + \boldsymbol{\beta}_i^T\boldsymbol{u}_i]TR_{fi} + \left\{1 + \boldsymbol{\beta}_i^T\boldsymbol{u}_i + [1 + \boldsymbol{\beta}_i^T\boldsymbol{u}_i]TR_{fi}\right\}I_{fi} \\ &\quad + \left\{1 + \boldsymbol{\beta}_i^T\boldsymbol{u}_i + [1 + \boldsymbol{\beta}_i^T\boldsymbol{u}_i]TR_{fi} + \left\{1 + \boldsymbol{\beta}_i^T\boldsymbol{u}_i + [1 + \boldsymbol{\beta}_i^T\boldsymbol{u}_i]TR_{fi}\right\}I_{fi}\right\}f_{ai}\end{aligned} \tag{47}$$

which we can use to set up our pseudo-range rate equation

$$\begin{aligned}\dot{\rho}_{r_i} &= c\left[\frac{\Delta f_{r_i}}{f_t}\right] \\ &= \boldsymbol{v}_{r_i/T}^T\boldsymbol{u}_i + \left[c + \boldsymbol{v}_{r_i/T}^T\boldsymbol{u}_i\right]TR_{fi} + \left\{c + \boldsymbol{v}_{r_i/T}^T\boldsymbol{u}_i + \left[c + \boldsymbol{v}_{r_i/T}^T\boldsymbol{u}_i\right]TR_{fi}\right\}I_{fi} \\ &\quad + \left\{\boldsymbol{v}_{r_i/T}^T\boldsymbol{u}_i + \left[c + \boldsymbol{v}_{r_i/T}^T\boldsymbol{u}_i\right]TR_{fi} + \left\{c + \boldsymbol{v}_{r_i/T}^T\boldsymbol{u}_i + \left[c + \boldsymbol{v}_{r_i/T}^T\boldsymbol{u}_i\right]TR_{fi}\right\}I_{fi}\right\}f_{ai}\end{aligned} \tag{48}$$

where $\dot{\rho}_{r_i}$ is the receiver to transmitter pseudo-range rate. For simplicity let us define

$$\begin{aligned}a_i(t) &= \left[c + \boldsymbol{v}_{\frac{r_i}{T}}^T\boldsymbol{u}_i\right]TR_{fi} \\ b_i(t) &= \left\{c + \boldsymbol{v}_{\frac{r_i}{T}}^T\boldsymbol{u}_i + \left[c + \boldsymbol{v}_{\frac{r_i}{T}}^T\boldsymbol{u}_i\right]TR_{fi}\right\}I_{fi} \\ d_i(t) &= \left\{\boldsymbol{v}_{r_i/T}^T\boldsymbol{u}_i + \left[c + \boldsymbol{v}_{r_i/T}^T\boldsymbol{u}_i\right]TR_{fi} + \left\{c + \boldsymbol{v}_{r_i/T}^T\boldsymbol{u}_i + \left[c + \boldsymbol{v}_{r_i/T}^T\boldsymbol{u}_i\right]TR_{fi}\right\}I_{fi}\right\}f_{ai}\end{aligned} \tag{49}$$

Table 2 provides the order of magnitude for each error source for FDOA and FROA. Although the measurement frequency shift can be solved for, the frequency shifts from the troposphere and ionosphere cannot be solved for. This is due to the both the troposphere and ionosphere constantly changing. Similar to TDOA, the ionosphere and troposphere shift terms place a performance floor on the frequency based geolocation.

Table 2. Order of magnitude of each error source for frequency based geolocation

Error Sources	Delay w/o Model (Hz)	Can be Solved For?
Frequency Shift	Depends on System	Y
Tropospheric Shift	10^{-1}	N
Ionospheric Shift	1	N

For FDOA we difference the frequency shifts measured by two receivers leading to the equation

$$\begin{aligned}&c\frac{\Delta f_{r_j}}{f_T} - c\frac{\Delta f_{r_i}}{f_T} = \dot{\rho}_{r_j} - \dot{\rho}_{r_i} \\ &= \boldsymbol{v}_{r_j/T}^T\boldsymbol{u}_j - \boldsymbol{v}_{r_i/T}^T\boldsymbol{u}_i + a_j(t) - a_i(t) + b_j(t) - b_i(t) + d_j(t) - d_i(t)\end{aligned} \tag{50}$$

We can now expand Eq. 50 to a polynomial in terms of transmitter position and the frequency measurement error for both receivers. However, this leads to a twelfth order polynomial with over 2000 terms. This polynomial is clearly intractable and an alternate method may need to be explored. If the error terms are ignored the resulting polynomial is still eighth order with over 100 terms. Another problem facing FDOA is the required knowledge of the carrier frequency of the transmitter. In our scenario, this may be difficult or impossible to know. With these issues facing FDOA, we may want to utilize Frequency Ratio of Arrival (FROA) instead.

3.3.6 FROA Equation

In FROA we will take the ratio of the frequency shifts measured by both receivers. Using Eq. 48 we get the FROA equation

$$\frac{\dot{\rho}_{r_j}}{\dot{\rho}_{r_i}} = \frac{\boldsymbol{v}_{r_{j/T}}^T \boldsymbol{u}_j + a_j(t) + b_j(t) + d_j(t)}{\boldsymbol{v}_{r_{i/T}}^T \boldsymbol{u}_i + a_i(t) + b_i(t) + d_i(t)} \tag{51}$$

To solve this equation, it is required to know the carrier frequency of the transmitter. To remove this requirement, we take the ratio of Eq. 47 for both satellites

$$\frac{f_{r_j}}{f_{r_i}} = \zeta_{j/i} = \frac{c + \boldsymbol{v}_{r_{j/T}}^T \boldsymbol{u}_j + a_j(t) + b_j(t) + d_j(t)}{c + \boldsymbol{v}_{r_{i/T}}^T \boldsymbol{u}_i + a_i(t) + b_i(t) + d_i(t)} \tag{52}$$

Taking into account frequency measurement error from both orbiting receivers we can expand Eq. 52 into a twelfth order polynomial with over 2000 terms. If we disregard the measurement error we can expand Eq. 52 into

$$\begin{aligned} 0 = &\left\{\boldsymbol{v}_{r_{j/T}}^T \left[\boldsymbol{r}_{T/r_j}\ \boldsymbol{r}_{T/r_j}^T\right] \boldsymbol{v}_{r_{j/T}}\right\} \boldsymbol{r}_{T/r_i}^T \boldsymbol{r}_{T/r_i} + \zeta_{j/i}^2 \left\{\boldsymbol{v}_{r_{i/T}}^T \left[\boldsymbol{r}_{T/r_i}\ \boldsymbol{r}_{T/r_i}^T\right] \boldsymbol{v}_{r_{i/T}}\right\} \boldsymbol{r}_{T/r_j}^T \boldsymbol{r}_{T/r_j} \\ &- 2\zeta_{j/i} \left[\boldsymbol{v}_{r_{j/T}}^T \boldsymbol{r}_{T/r_j}\right] \left[\boldsymbol{v}_{r_{i/T}}^T \boldsymbol{r}_{T/r_i}\right] \|\boldsymbol{r}_{T/r_i}\| \left\|\boldsymbol{r}_{T/r_j}\right\| \\ &- c^2 \left[\boldsymbol{r}_{T/r_i}^T \boldsymbol{r}_{T/r_i}\right] \left[\boldsymbol{r}_{T/r_j}^T \boldsymbol{r}_{T/r_j}\right] \left[\zeta_{j/i} - 1\right]^2 \end{aligned} \tag{53}$$

Expanding Eq. 53 provides an eighth order polynomial. This is a very similar result to the FDOA polynomials where both polynomials generated are intractable and are in need of an alternative method.

3.3.7 FROA/TDOA Hybrid Polynomial

Here we derive a method that utilizes a hybrid polynomial that uses both TDOA and FROA equations. We begin by expanding Eq. 52, ignoring frequency measurement error and atmospheric error, to get the equation

$$0 = \boldsymbol{v}_{r_{j/T}}^T \boldsymbol{r}_{T/r_j} \|\boldsymbol{r}_{T/r_i}\| - \zeta_{j/i} \boldsymbol{v}_{r_{i/T}}^T \boldsymbol{r}_{T/r_i} \left\|\boldsymbol{r}_{T/r_j}\right\| - c\|\boldsymbol{r}_{T/r_i}\| \left\|\boldsymbol{r}_{T/r_j}\right\| \left[\zeta_{j/i} - 1\right] \tag{54}$$

We then ignore the error in Eq. 27 to get

$$\Delta r_{ji} = \left\|\boldsymbol{r}_{T/r_j}\right\| - \|\boldsymbol{r}_{T/r_i}\| \tag{55}$$

which we can now perform simple algebra and rearrange to be

$$\left\|\boldsymbol{r}_{T/r_j}\right\| \left\|\boldsymbol{r}_{T/r_i}\right\| = \frac{1}{2}\left[\boldsymbol{r}_{T/r_j}^T \boldsymbol{r}_{T/r_j} + \boldsymbol{r}_{T/r_i}^T \boldsymbol{r}_{T/r_i} - \Delta r_{ji}^2\right] \tag{56}$$

We can also perform simple mathematics and rearrangement on Eq. 56 to get the equations

$$\left\|\boldsymbol{r}_{T/r_j}\right\| = \frac{1}{2\Delta r_{ji}}\left[\boldsymbol{r}_{T/r_j}^T \boldsymbol{r}_{T/r_j} + \Delta r_{ji}^2 - \boldsymbol{r}_{T/r_i}^T \boldsymbol{r}_{T/r_i}\right] \tag{57}$$

and

$$\left\|\boldsymbol{r}_{T/r_i}\right\| = \frac{1}{2\Delta r_{ji}}\left[\boldsymbol{r}_{T/r_i}^T \boldsymbol{r}_{T/r_i} + \Delta r_{ji}^2 - \boldsymbol{r}_{T/r_j}^T \boldsymbol{r}_{T/r_j}\right] \tag{58}$$

Substituting Eqs. 56, 57, and 58 into Eq. 53 we get the equation

$$\begin{aligned} 0 = \boldsymbol{v}_{r_j/T}^T \boldsymbol{r}_{T/r_j} & \frac{1}{2\Delta r_{ji}}\left[\boldsymbol{r}_{T/r_i}^T \boldsymbol{r}_{T/r_i} + \Delta r_{ji}^2 - \boldsymbol{r}_{T/r_j}^T \boldsymbol{r}_{T/r_j}\right] \\ & - \zeta_{j/i} \boldsymbol{v}_{r_i/T}^T \boldsymbol{r}_{T/r_i} \frac{1}{2\Delta r_{ji}}\left[\boldsymbol{r}_{T/r_j}^T \boldsymbol{r}_{T/r_j} + \Delta r_{ji}^2 - \boldsymbol{r}_{T/r_i}^T \boldsymbol{r}_{T/r_i}\right] \\ & - c\frac{1}{2}\left[\boldsymbol{r}_{T/r_j}^T \boldsymbol{r}_{T/r_j} + \boldsymbol{r}_{T/r_i}^T \boldsymbol{r}_{T/r_i} - \Delta r_{ji}^2\right]\left[\zeta_{j/i} - 1\right] \end{aligned} \tag{59}$$

For simplicity let us define the three variables

$$\begin{aligned} \epsilon &= \boldsymbol{r}_{T/r_i}^T + \boldsymbol{r}_{T/r_j}^T \\ \xi &= \boldsymbol{r}_{T/r_j}^T \boldsymbol{r}_{T/r_j} + \boldsymbol{r}_{T/r_i}^T \boldsymbol{r}_{T/r_i} \\ \eta &= \xi I_{3\times 3} + 2\,\boldsymbol{r}_{T/r_j}\,\boldsymbol{r}_{T/r_j}^T + 2\,\boldsymbol{r}_{T/r_i}\,\boldsymbol{r}_{T/r_i}^T \end{aligned} \tag{60}$$

where $I_{3\times 3}$ is the identity matrix. We can expand Eq. 60 using Eq. 29 and then rearrange into

$$0 = \boldsymbol{r}_T^T A \boldsymbol{r}_T + B^T \boldsymbol{r}_T - C \tag{61}$$

where A, B, and C are

$$
\begin{aligned}
A &= \frac{1}{\Delta r_{ji}}\{\zeta_{j/i}\boldsymbol{v}_{r_i/T} - \boldsymbol{v}_{r_i/T}\}\epsilon - c[\zeta_{j/i} - 1]I_{3\times 3} \\
B^T &= \frac{1}{2\Delta r_{ji}}\{\boldsymbol{v}_{r_j/T}[\eta - \Delta r_{ji}^2 I_{3\times 3}] - \zeta_{j/i}\boldsymbol{v}_{r_i/T}^T[\eta - \Delta r_{ji}^2 I_{3\times 3}]\} + c[\zeta_{j/i} - 1]\epsilon \\
C &= \frac{1}{2\Delta r_{ji}}\left[\zeta_{j/i}\boldsymbol{v}_{r_i/T}^T\boldsymbol{r}_{T/r_i} - \boldsymbol{v}_{r_j/T}^T\boldsymbol{r}_{T/r_j}\right][\xi + \Delta r_{ji}^2] - \frac{1}{2}c[\zeta_{j/i} - 1][\xi + \Delta r_{ji}^2]
\end{aligned}
\tag{62}
$$

Equation 57 can then be expanded to a second order polynomial in terms of (x_t, y_t, z_t).

3.4 Sequential Estimation with an Extended Kalman Filter (EKF)

The measurement types discussed in the prior sections (e.g., MUSIC, TDOA, FDOA) may be used for either initial orbit determination (IOD) or precise orbit determination (POD). If the objective is POD, we further have the option of processing the measurements as a group (the so-called batch processing approach) or processing the measurements sequentially. After conversations with the sponsor, we decided the sequential option was of most interest and chose to accomplish this via an extended Kalman filter (EKF).

After the Kalman filter's initial development in the 1960s, it was quickly expanded into the EKF to handle situations with non-linear measurement models and non-linear dynamics. The details of an EKF are well understood and the interested reader is directed to a number of excellent texts on this topic, including Refs. [39], [40], and [41]. Moreover, the application of the EKF to sequential estimation of a spacecraft's state is also well understood and well documented. Verbose explanations of all the requisite equations and concepts may be found in popular texts such as [42] or [43]. These ideas are further expanded upon in a recent NASA-published document on "best practices" for spacecraft navigation [44]. The EKF implemented for this work is entirely consistent with the conventions laid out in the references cited here.

The EKF designed and implemented as part of this work is a proof-of-concept filter, intended primary to explore the POD performance possible using only MUSIC measurements. The scenario investigated here is for a single transmitter in low Earth orbit (LEO) and a single receiver in a different orbit. The filter state is comprised of the position and velocity of the transmitter, since we assume the state of the receiver is known. As a proof-of-concept, the filter dynamics are governed by Keplerian motion (i.e., two-body orbital dynamics), though we do account for a representative amount of random accelerations as process noise.

Measurements are obtained by simulating the RF signal at the receiver location, which consists of a primary signal (from an arbitrary direction) and an interfering signal from the unknown transmitter. We assume each of these signals have a different signal-to-noise ratio (SNR), which is used to corrupt each of these ideal signals. The corrupted plane wave is then sampled and passed to the MUSIC algorithm, which returns the bearing (i.e., direction) to the two sources. Since we presume the primary signal originates from a known asset, we can determine which bearing measurement is associated with the unknown transmitter---and it is this measurement that is passed to the EKF for POD.

4 RESULTS AND DISCUSSION

4.1 MUSIC Algorithm Analysis Results

We performed an analysis of the MUSIC algorithm for both single and two signal cases. We developed a set of scenarios for each case. Each scenario would result in a contour plot of bearing angle error and would be used to determine the MUSIC algorithm's sensitivity to certain signal and sensor array properties. Each point on the contour plot is determined using a Monte Carlo analysis where random noise of a certain power, determined by the Signal-to-Noise Ratio (SNR), was added to the received signal. Each Monte Carlo analysis provides the mean and standard deviation of the bearing angle error between the estimated DOA and true DOA.

4.1.1 Single Signal Results

We began by analyzing the MUSIC algorithm with a set of scenarios involving a single signal. The first group of scenarios determined the algorithm’s sensitivity to signal’s azimuth and elevation. Each scenario used a different array geometry and number of elements and the defined parameters of these scenarios can be found in Table 3. Results are shown in Figure 3 to Figure 7.

Table 3. Parameters for group 1 scenarios for single signal MUSIC analysis

Scenario	Frequency	SNR (dB)	Number of Elements	Array Geometry
1	2.2 GHz	5	5x5	Uniform Rectangular Array
2	2.2 GHz	5	5x5	Rectangular Array with Offset
3	2.2 GHz	5	25	Uniform Circular Array
4	2.2 GHz	5	2x2	Uniform Rectangular Array
5	2.2 GHz	5	2x2	Rectangular Array with Offset

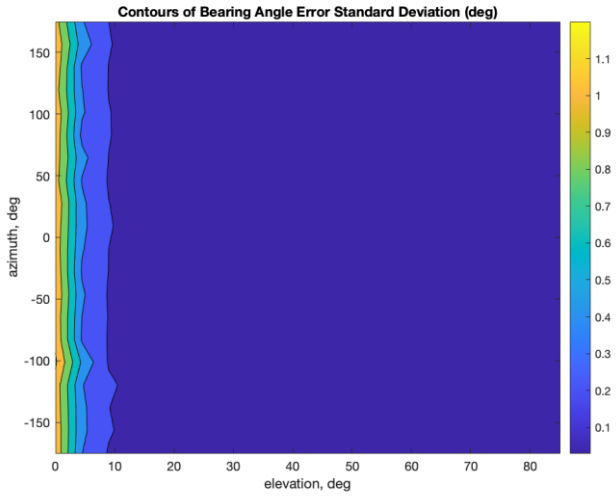

Figure 3. Monte Carlo result for group 1, scenario 1 for single signal MUSIC analysis

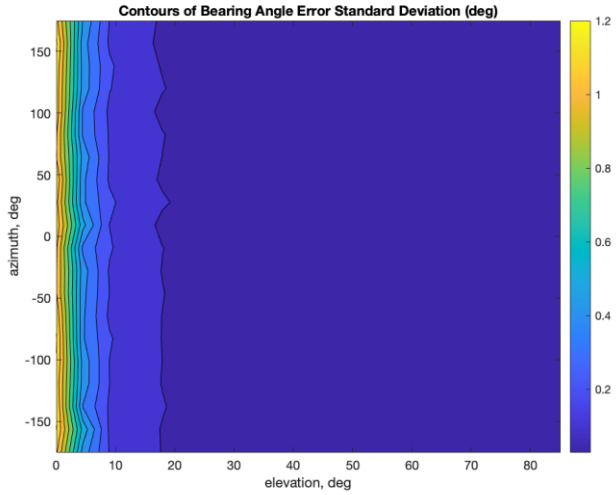

Figure 4. Monte Carlo result for group 1, scenario 2 for single signal MUSIC analysis

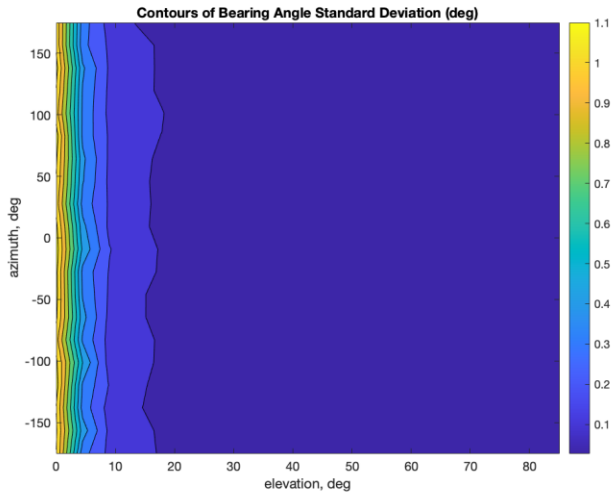

Figure 5. Monte Carlo result for group 1, scenario 3 for single signal MUSIC analysis

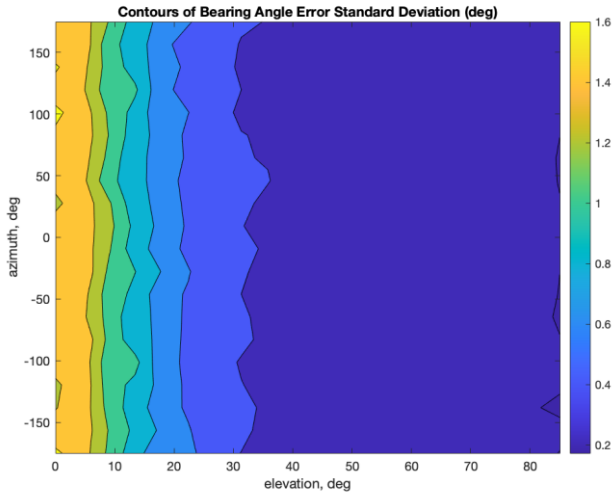

Figure 6. Monte Carlo result for group 1, scenario 4 for single signal MUSIC analysis

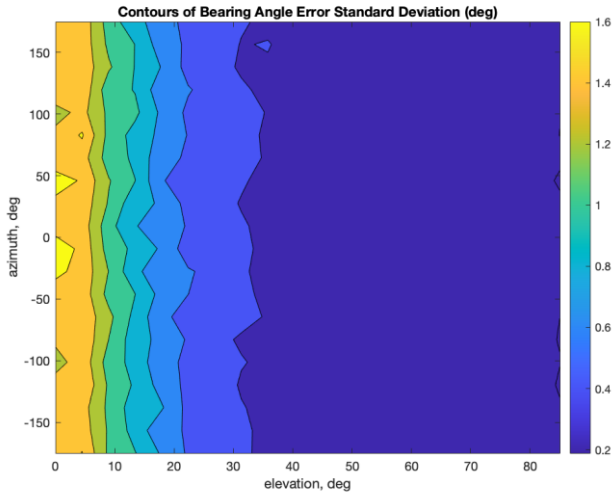

Figure 7. Monte Carlo result for group 1, scenario 5 for single signal MUSIC analysis

From these results, we can see that MUSIC is more sensitive to elevation of the incoming signal rather than the azimuth. A lower elevation for all array geometries provides a higher bearing angle error. Looking at Figures 6 and 7 we see that the bearing angle is larger when less receiver elements are used.

The second group of scenarios analyzed the algorithm's response to varying signal carrier frequency and Signal to Noise Ration (SNR). We define the parameters of this group in Table 4. Results are shown in Figure 8 and Figure 9.

Table 4. Parameters of group 2 scenarios for single signal MUSIC analysis

Scenarios	Azimuth of Signal (deg)	Elevation of Signal (deg)	Number of Elements	Array Geometry
1	0	85	5x5	Uniform Rectangular Array
2	45	45	5x5	Uniform Rectangular Array

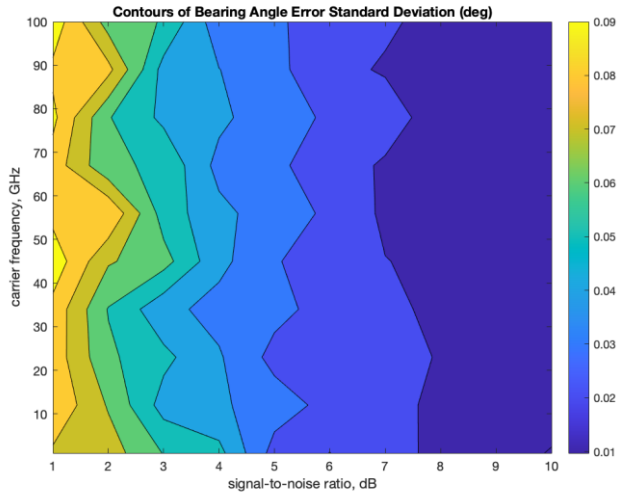

Figure 8. Monte Carlo result for group 2, scenario 1 for single signal MUSIC analysis

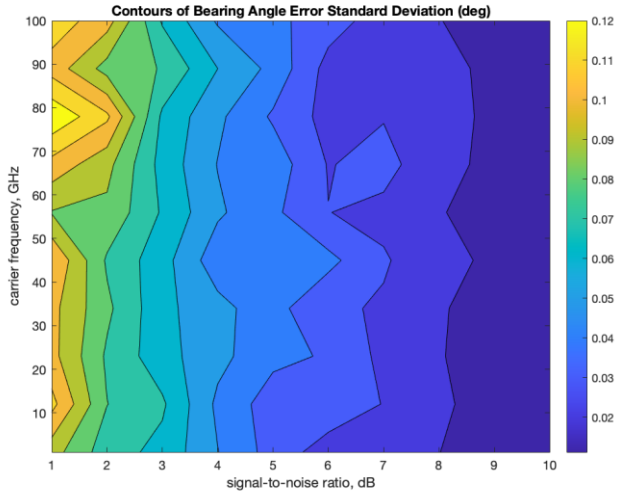

Figure 9. Monte Carlo result for group 2, scenario 2 for single signal MUSIC analysis

Figures 8 and 9 show us that MUSIC is more sensitive to SNR than carrier frequency.

We then analyzed MUSIC's response to sample frequency. The parameters for this third group of scenarios can be found in Table 5. Results are shown in Figure 10 to Figure 12.

Table 5. Parameters for group 3 scenarios for single signal MUSIC analysis

Scenario	Frequency	SNR (dB)	Azimuth of Signal (deg)	Elevation of Signal (deg)	Number of Elements	Array Geometry
1	2.2 GHz	5	0	85	5x5	Uniform Rectangular Array
2	2.2 GHz	5	45	45	5x5	Uniform Rectangular Array
3	2.2 GHz	5	45	45	2x2	Uniform Rectangular Array

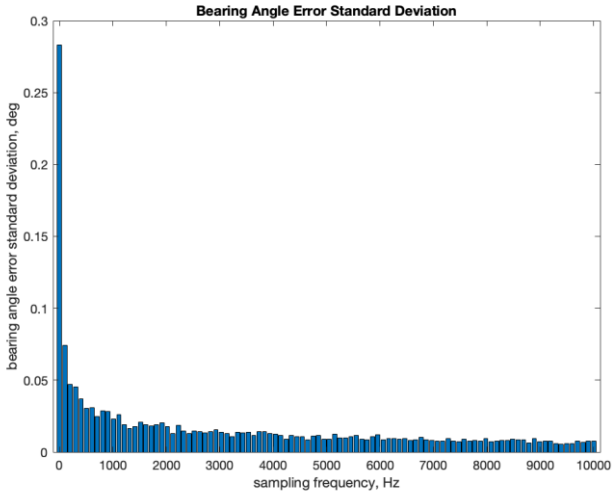

Figure 10. Monte Carlo result for group 3, scenario 1 for single signal MUSIC analysis

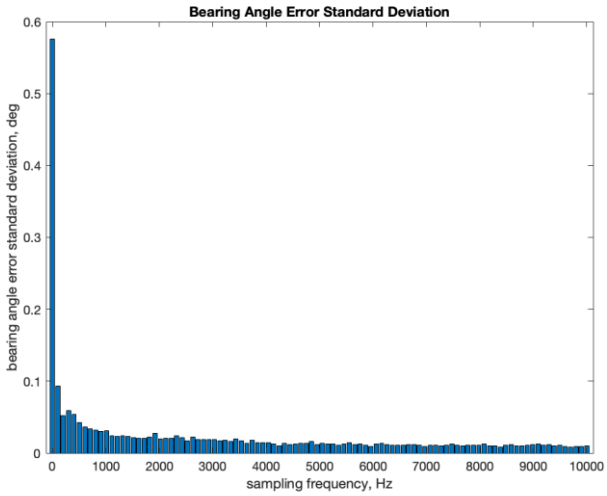

Figure 11. Monte Carlo result for group 3, scenario 2 for single signal MUSIC analysis

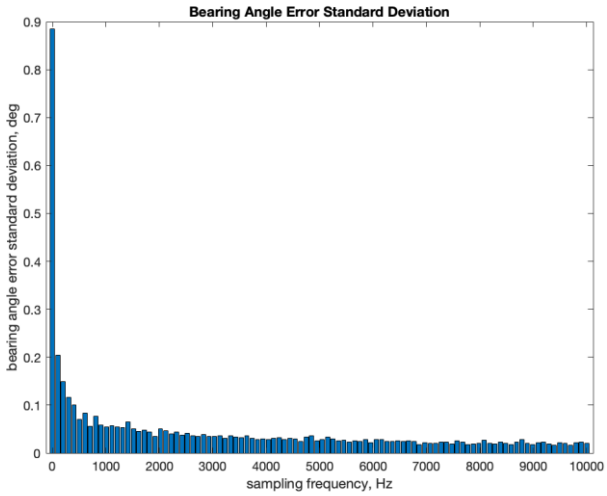

Figure 12. Monte Carlo result for group 3, scenario 3 for single signal MUSIC analysis

These results agree with our intuition that the higher the sampling frequency the lower the error in the DOA estimation.

Our previous results show that MUSIC is sensitive to the elevation of the signal and the SNR of the signal. Our last group of scenarios explores this by analyzing MUSIC's response to varying elevation and SNR. The parameters for this fourth and final group for single signal analysis can be found in Table 6. Results are shown in Figure 13 to Figure 15.

Table 6. Parameters for group 4 scenarios for single signal MUSIC analysis

Scenario	Frequency	Azimuth of Signal (deg)	Number of Elements	Array Geometry
1	2.2 GHz	0	2x2	Uniform Rectangular Array
2	2.2 GHz	0	5x5	Uniform Rectangular Array
3	2.2 GHz	0	10x10	Uniform Rectangular Array

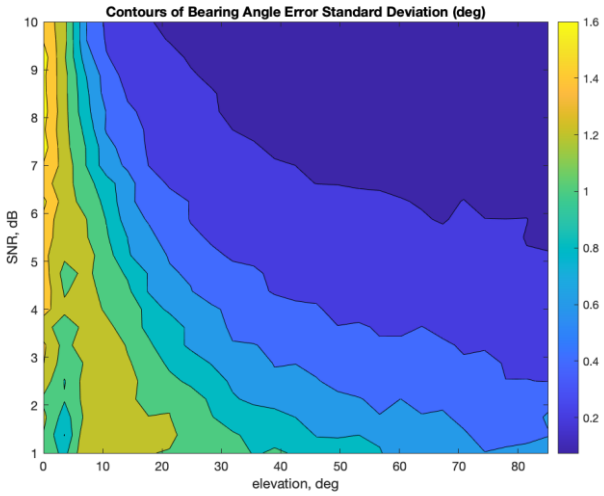

Figure 13. Monte Carlo result for group 4, scenario 1 for single signal MUSIC analysis

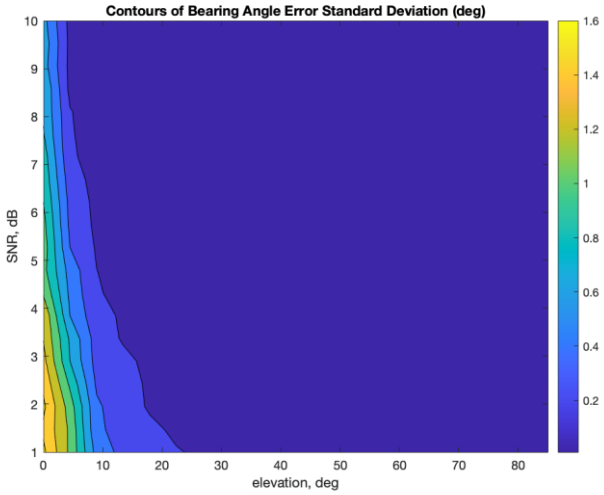

Figure 14. Monte Carlo result for group 4, scenario 2 for single signal MUSIC analysis

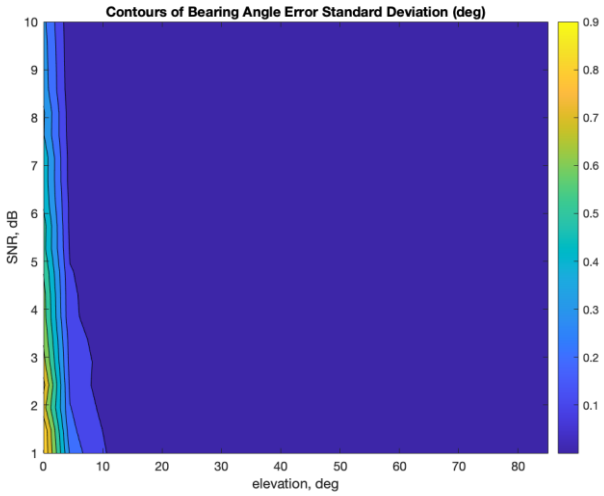

Figure 15. Monte Carlo result for group 4, scenario 3 for single signal MUSIC analysis

These results show that the algorithm has a higher error sensitivity to elevation than SNR.

4.1.2 Two-Signal Results

We performed two groups of scenarios for the two-signal analysis of the MUSIC algorithm. The first group analyzes the algorithm's sensitivity to varying angle between the signals and the power ratio between the two signals. The defined parameters provide an azimuth and elevation of the primary signal that we perform a DOA estimation on. The provided SNR is the ratio between the weaker signal (our primary signal) and noise. We can find the parameters in Table 7. Results are shown in Figure 16 to Figure 18.

Table 7. Parameters for group 1 for two-signal MUSIC Analysis

Scenario	Frequency	SNR (dB)	Azimuth of Signal (deg)	Elevation of Signal (deg)	Number of Elements	Array Geometry
1	2.2 GHz	1	45	45	5x5	Uniform Rectangular Array
2	2.2 GHz	5	45	45	5x5	Uniform Rectangular Array
3	2.2 GHz	10	45	45	5x5	Uniform Rectangular Array

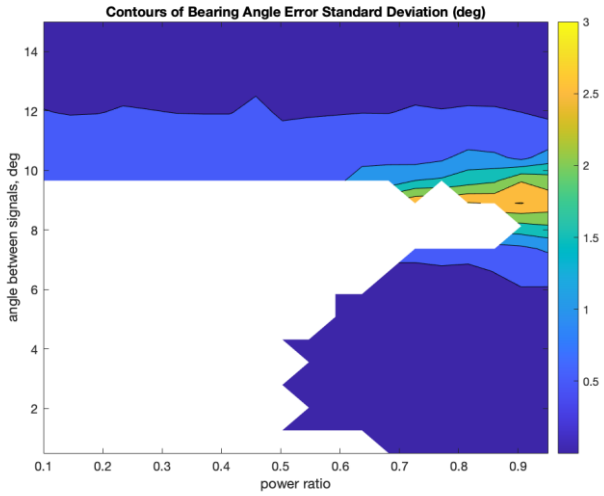

Figure 16. Monte Carlo result for group 1, scenario 1 for two-signal MUSIC analysis

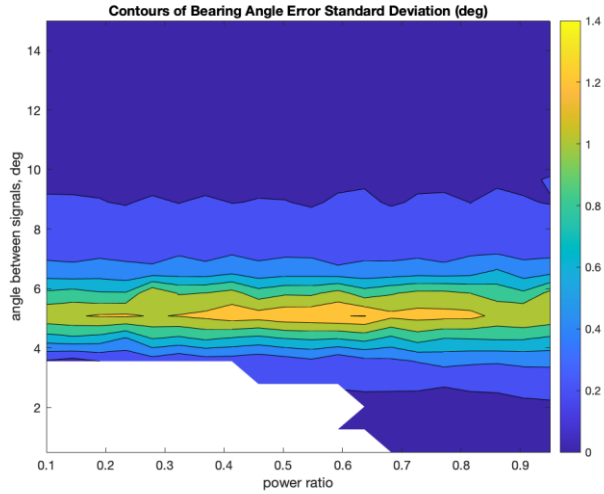

Figure 17. Monte Carlo result for group 1, scenario 2 for two-signal MUSIC analysis

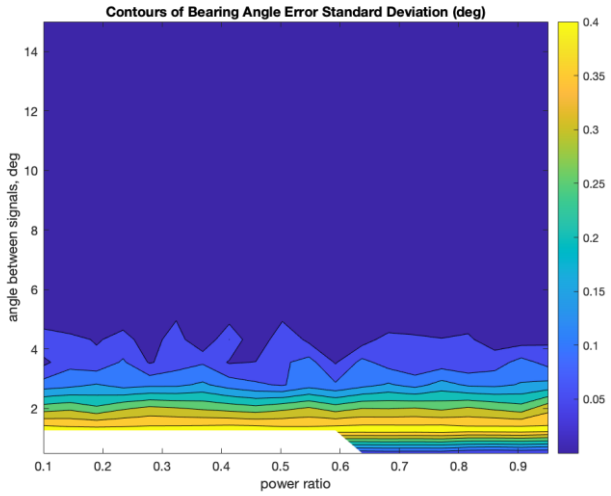

Figure 18. Monte Carlo result for group 1, scenario 3 for two-signal MUSIC analysis

We found in these results that when the angle between two signals is small enough, the algorithm has a difficulty in separating the two angles. That is why there are areas in the plots that are white. Rather than producing two DOA, one for each signal, the algorithm may produce only one DOA.

Similar to the first group in the single signal analysis, our second group of scenarios analyzes MUSIC's response to varying azimuths and elevations of the primary signal. We also vary the array geometry in each scenario. The parameters for this group can be found in Table 8. Results are shown in Figure 19 to Figure 21

Table 8. Parameters for group 2 for two-signal MUSIC Analysis

Scenario	Frequency	SNR (dB)	Power Ratio	Angle Between Signals (deg)	Number of Elements	Array Geometry
1	2.2 GHz	10	0.5	5	5x5	Uniform Rectangular Array
2	2.2 GHz	10	0.5	5	5x5	Rectangular Array with Offset
3	2.2 GHz	10	0.5	5	25	Uniform Circular Array

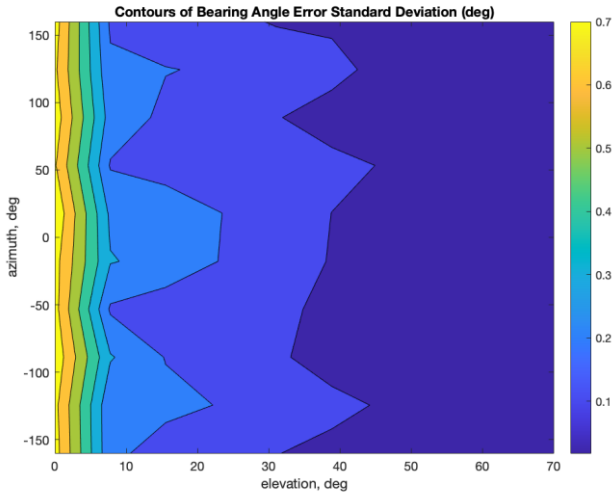

Figure 19. Monte Carlo result for group 2, scenario 1 for two-signal MUSIC analysis

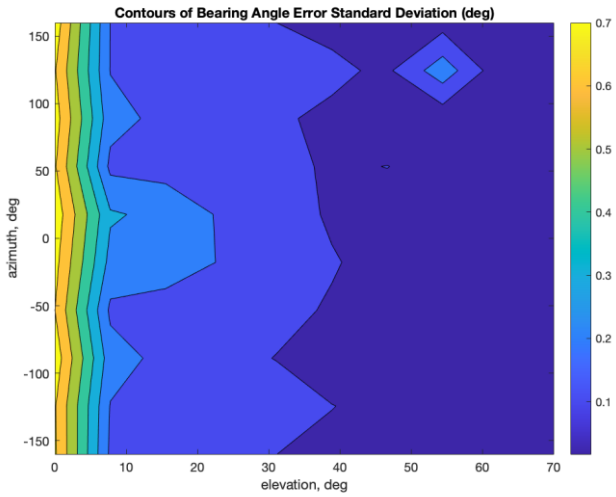

Figure 20. Monte Carlo result for group 2, scenario 2 for two-signal MUSIC analysis

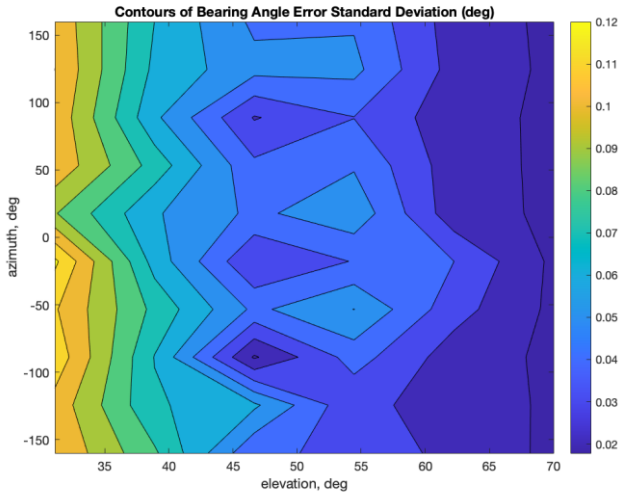

Figure 21. Monte Carlo result for group 2, scenario 2 for two-signal MUSIC analysis

We find that the MUSIC is more sensitive to elevation of the primary signal rather than its azimuth. This is similar to the results of the first group of scenarios for the single signal cases.

4.2 Geolocation with TDOA and FROA Results (Root Locus Analysis)

Root locus is used extensively in modern control systems for the development of compensators. The modern root locus method analyzes migration of the characteristic equation's (a polynomial) roots as a single parameter is varied. Instead of adjusting one parameter, our analysis involves adjusting multiple parameters in a polynomial system to better understand the effect on the system's solutions. We visualize this by plotting a root locus of each of the variables in the polynomial system.

Our goal is to visualize the effects of error added to the TDOA and FROA measurements on the solution to their respective polynomials. We begin by developing a TDOA or FROA/TDOA polynomial system for each scenario. We then perform a Monte Carlo simulation of the geometric only TDOA and FROA/TDOA hybrid polynomial systems adding error to each measurement. We plot the roots of the system for each of the 300 trials of the Monte Carlo simulation.

Information on our two scenarios can be found in Tables 9 and 10. These tables provide transmitter and satellite information. The large (X) markers in our root locus plots represent the zero error solutions with the red solution being the true solution. All other solutions are represented by blue or gray dots. Blue dots are solutions that satisfy the original TDOA equation or both TDOA and FROA equation we refer to these as *valid solutions*. Gray dots represent *extraneous solutions* that satisfy the final polynomial, but do not satisfy the original equations. Extraneous solutions are introduced when the original TDOA or FROA equations are squared to arrive at a polynomial representation of the problem.

Table 9. Transmitter location and measurement times for scenario 1 and 2

Scenario	Date	Time	Ground Information		Measurement Times (s)		
			Latitude	Longitude	t1	t2	t3
1	10/31/2019	17:00:00	42.7 N	73.7 W	428	988	1548
2	10/31/2019	17:00:00	42.7 N	73.7 W	386	1000	1614

Table 10. Satellite 1 and 2's orbital parameters for scenario 1 and 2

Satellite 1 Parameters						
Scenario	Semi-Major Axis (km)	Eccentricity (~)	Inclination (deg)	RAAN (deg)	Argument of Perigee (deg)	True Anomaly (deg)
1	8000	0.05	55	180	0	0
2	8000	0.05	71	196	0	0
Satellite 2 Parameters						
Scenario	Semi-Major Axis (km)	Eccentricity (~)	Inclination (deg)	RAAN (deg)	Argument of Perigee (deg)	True Anomaly (deg)
1	8000	0.05	55	180	0	15
2	8000	0.05	50	172	19	0

We begin by plotting the root locus results for scenario 1 in Figures 22, 23, 24, and 25. We can see that there is no interaction between the real roots for the TDOA polynomial (Figures 22 and 23). We see in Figure 22 there are two groups of valid solutions (blue dots), one surrounding the true position of the transmitter and the other surrounding an extraneous solution. Two real roots of the FROA/TDOA polynomial (Figures 24 and 25) seem to migrate towards each other and move to the imaginary axis. This means there are instances where error added to the measurements drives the polynomial to provide zero real or valid solutions.

We then plot the root locus results for scenario 2 in Figures 26, 27, 28, and 29. Similar to scenario 1, we see that the TDOA solutions do not migrate as far as the FROA/TDOA polynomial. This may be due to the addition of error to both TDOA and FROA measurements. We also see that the error added to the FROA measurements is much smaller than the error added to the TDOA and there is more migration of the FROA/TDOA polynomial roots than the TDOA polynomial roots. This suggests that the hybrid polynomial may be more sensitive to error in FROA measurements than in the TDOA measurements. Comparing Figures 26 and 28 to Figures 22 and 24 we see more of a point cloud on some of the roots in the imaginary plane for scenario 2 than in scenario 1.

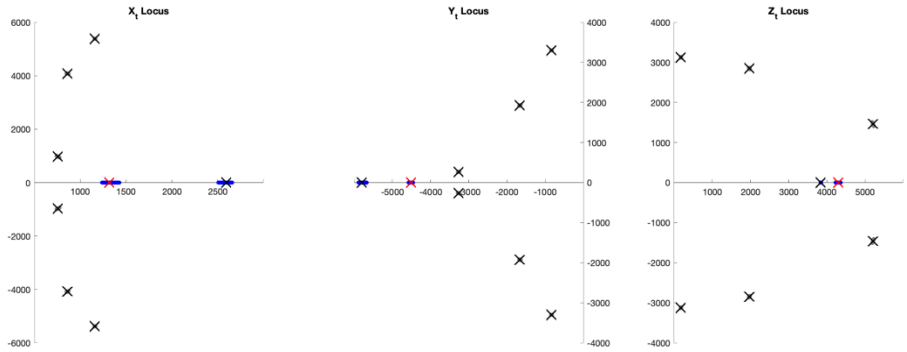

Figure 22. Scenario 1 root locus results with 1 km error applied to TDOA measurement for TDOA polynomial

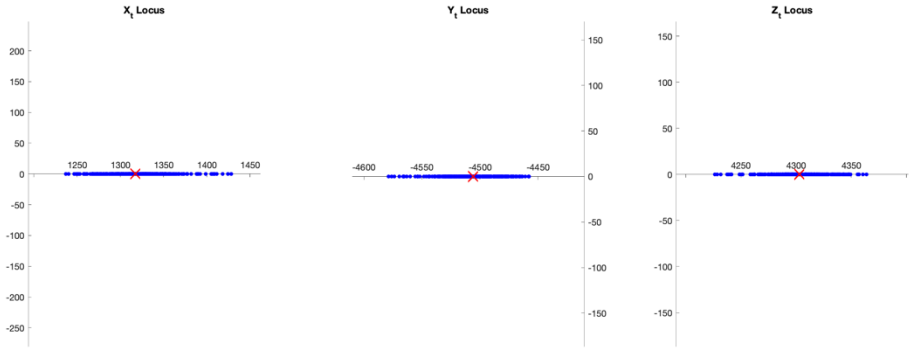

Figure 23. Zoom-in of Figure 22 about the true solution

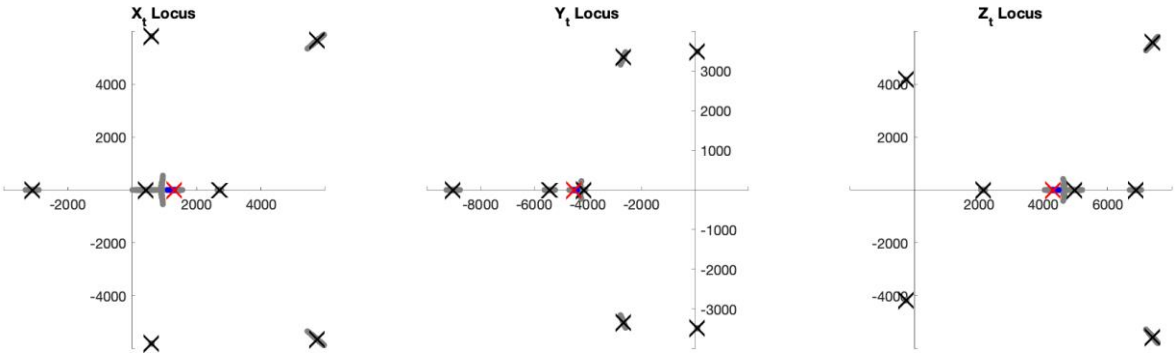

Figure 24. Scenario 1 root locus results with 100 m error applied to TDOA measurement and frequency ratio error of 3×10^{-8} for FROA/TDOA polynomial

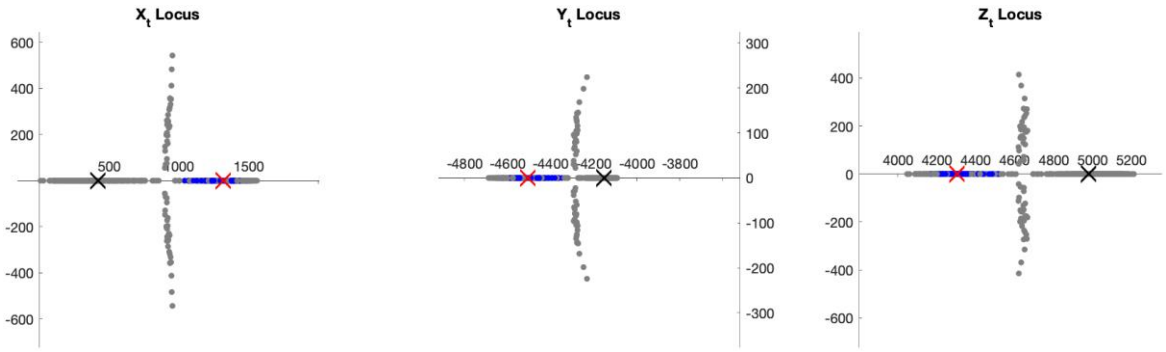

Figure 25. Zoom-in of Figure 24 showing the interaction between the true root and the extraneous root

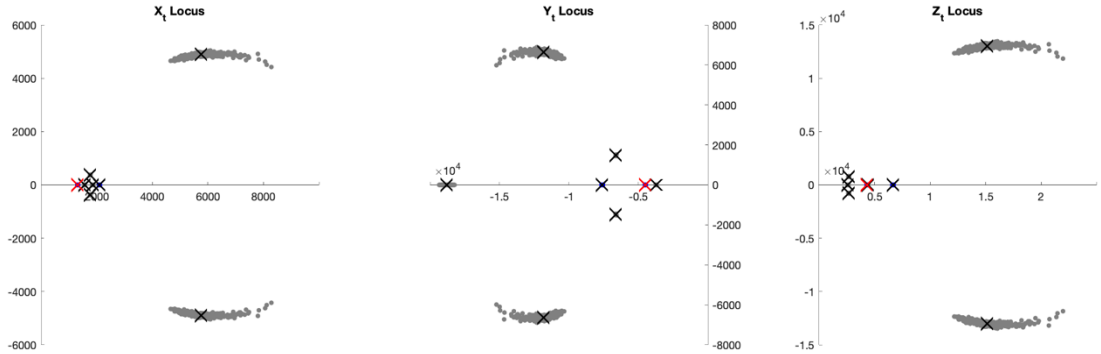

Figure 26. Scenario 2 root locus results with 1 km error applied to TDOA measurement for TDOA polynomial

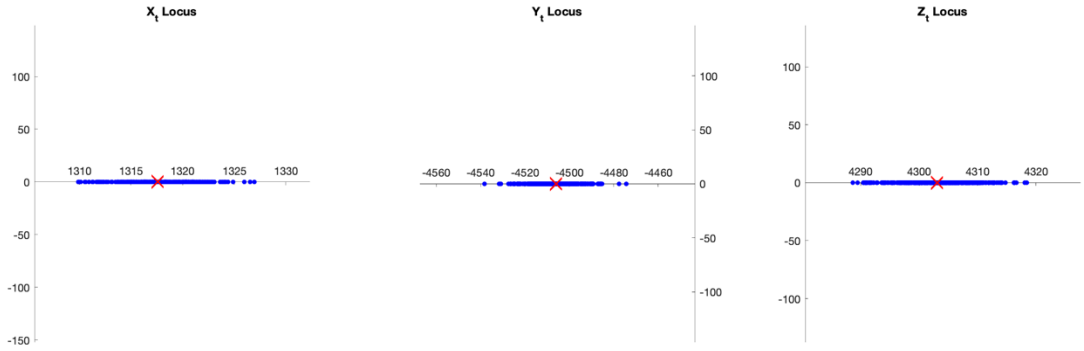

Figure 27. Zoom-in of Figure 26 about the true solution

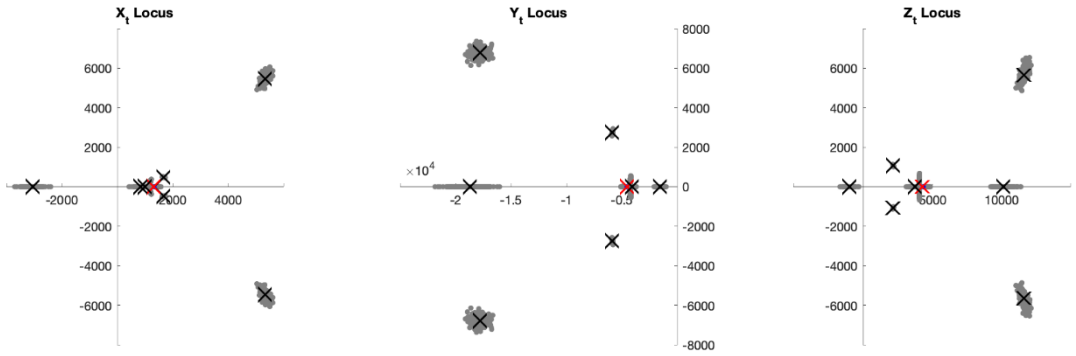

Figure 28. Scenario 2 root locus results with 100m error applied to TDOA measurement and a frequency ration error of 3×10^{-8} for FROA/TDOA polynomial

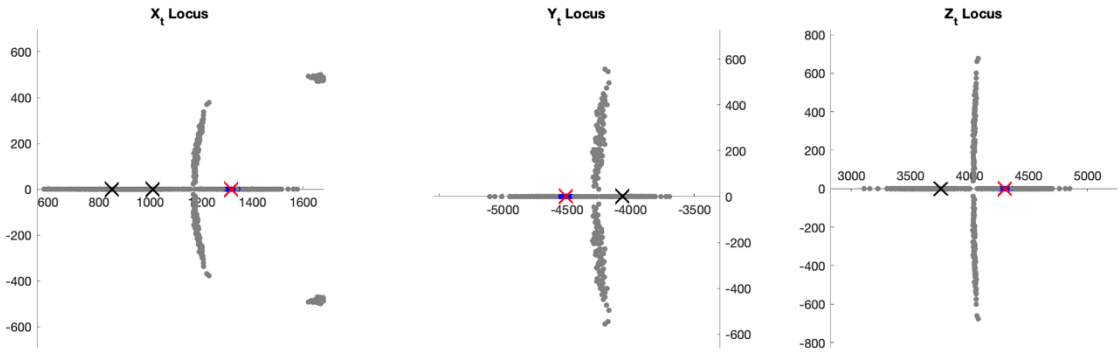

Figure 29. Zoom-in of Figure 28 showing the interaction between the true root and the extraneous root

4.3 Initial Orbit Determination (IOD) with Frequency Based Observables

We analyzed the existence and uniqueness of Doppler-based orbit determination. In the case of seven (or more) concurrent measurements, we have shown a solution to exist and be locally unique for a transmitter and receivers in general position. There are specific degenerate geometries leading to ambiguous (non-unique) solutions, such as a "string of pearls" orbital configuration or all elements along a line. Both of these degenerate configurations may often be avoided in practice.

Existence and uniqueness of non-concurrent measurements is more challenging. While we have not yet shown this analytically (for two body motion), we have demonstrated local uniqueness numerically. Under the situation where a reasonable initial guess of the transmitter's orbit is known, we have shown that a simple gradient-based method may be used to find the transmitter's actual orbit.

4.3.1 Manipulation of the Doppler Equation for IOD

Let's first consider the first order Doppler measurement

$$f = \left(1 - \frac{\boldsymbol{v}^T \boldsymbol{u}}{c}\right) f_T \tag{63}$$

where f is the measured frequency, f_T is the carrier frequency, c is the speed of light, $\boldsymbol{v}$ is the relative velocity between the transmitter and the receiver, and $\boldsymbol{u}$ is the unit vector pointing from the receiver to the transmitter and can be expressed as

$$\boldsymbol{u} = \frac{\boldsymbol{r}}{r} \tag{64}$$

where $\boldsymbol{r}$ is the position of the transmitter relative to the position of the receiver. We will express the relative velocity as

$$\boldsymbol{v} = \boldsymbol{v}_T - \boldsymbol{v}_R \tag{65}$$

where $[\ ]_T$ and $[\ ]_R$ will denote the transmitter and the receiver respectively. We will also express the relative position as

$$\boldsymbol{r} = \boldsymbol{r}_T - \boldsymbol{r}_R \tag{66}$$

The Doppler equation can be rearranged into

$$c\left(\frac{\Delta f}{f_T}\right) = -\boldsymbol{v}^T \boldsymbol{u} = -(\boldsymbol{v}_T - \boldsymbol{v}_R)^T \frac{\boldsymbol{r}_T - \boldsymbol{r}_R}{\|\boldsymbol{r}_T - \boldsymbol{r}_R\|} \tag{67}$$

4.3.2 IOD from Concurrent Frequency Measurements

Let's begin by setting up a system of nonlinear equations of the form $S(\boldsymbol{x}) = 0$. Using Eq. 67 we choose to define S as

$$S = \begin{matrix} \left(\frac{f_{R1} - f_T}{f_T}\right) = -\boldsymbol{v}^T \boldsymbol{u} = -(\boldsymbol{v}_T - \boldsymbol{v}_{R1})^T \frac{\boldsymbol{r}_T - \boldsymbol{r}_{R1}}{\|\boldsymbol{r}_T - \boldsymbol{r}_{R1}\|} \\ \vdots \\ \left(\frac{f_{Rk} - f_T}{f_T}\right) = -\boldsymbol{v}^T \boldsymbol{u} = -(\boldsymbol{v}_T - \boldsymbol{v}_{Rk})^T \frac{\boldsymbol{r}_T - \boldsymbol{r}_{Rk}}{\|\boldsymbol{r}_T - \boldsymbol{r}_{Rk}\|} \end{matrix} \tag{68}$$

Our knowns in these systems of equations include the position and velocity of each receiver, $\{\boldsymbol{r}_{r_i}, \boldsymbol{v}_{r_i}\}_{i=1}^{k}$. Our observables are the frequency measured by each receiver at a certain time, t. The unknowns include the position, velocity, and the carrier frequency of the transmitter. For the perfect measurement case, the measured frequency of each receiver is related to the position and velocity of the receiver and the position, velocity, and frequency of the transmitter by Eq. 63. There are seven unknown states for a generic 3D orbit with an unknown transmitter frequency. Therefore, recognizing that each RF measurement corresponds to a 1D equation for the observed frequency, a minimum of $k = 7$ measurements are required to solve for the unknowns. We must also impose the requirement that none of the receivers is coincident with the transmitter.

The proof that a solution exists is trivial for perfect measurements. We know from Eq. 63 that the frequency measured by a receiver is related to the relative velocity, relative position, and the frequency of the transmitter. Because of this relation the position, velocity, and the frequency of the transmitter will always solve the system of equations. Unfortunately, the frequency measurements at our receivers are noisy and our knowledge of the receiver states (position and velocity) are not perfect. Future work will involve deriving a proof that a real solution exists for the perturbed measurement case.

Although it is difficult to prove global uniqueness of a solution to a set of nonlinear equations, we can prove local uniqueness of the solution by invoking the Inverse Function Theorem [45] [46]. The theorem states that a system of equations, $S(\boldsymbol{x}) = y$, has a unique solution for a neighborhood about a point $\boldsymbol{x}_0$ if the Jacobi matrix of S at point $\boldsymbol{x_0}$ is non-singular. We will define the Jacobi matrix as

$$J = \begin{bmatrix} \frac{dS_1}{d\boldsymbol{r}_T} & \frac{dS_1}{d\boldsymbol{v}_T} & \frac{dS_1}{df_T} \\ \vdots & \vdots & \vdots \\ \frac{dS_7}{d\boldsymbol{r}_T} & \frac{dS_7}{d\boldsymbol{v}_T} & \frac{dS_7}{df_T} \end{bmatrix} \tag{69}$$

From Eq. 68 we know that

$$S_i(\boldsymbol{r}_T, \boldsymbol{v}_T, f_T) = c\left(\frac{\Delta f_i}{f_T}\right) + \left(\boldsymbol{v}_T - \boldsymbol{v}_{R_i}\right)^T \frac{\boldsymbol{r}_T - \boldsymbol{r}_{R_i}}{\left\|\boldsymbol{r}_T - \boldsymbol{r}_{R_i}\right\|} \tag{70}$$

We will begin by taking the derivative of S_i with respect to $\boldsymbol{r}_T$ which gives us

$$\frac{dS_i}{d\boldsymbol{r}_T} = \frac{\left(\boldsymbol{v}_T - \boldsymbol{v}_{R_i}\right)^T}{\left[\left(\boldsymbol{r}_T - \boldsymbol{r}_{R_i}\right)^T\left(\boldsymbol{r}_T - \boldsymbol{r}_{R_i}\right)\right]^{1/2}} - \frac{\left(\boldsymbol{v}_T - \boldsymbol{v}_{R_i}\right)^T\left(\boldsymbol{r}_T - \boldsymbol{r}_{R_i}\right)\left(\boldsymbol{r}_T - \boldsymbol{r}_{R_i}\right)^T}{\left[\left(\boldsymbol{r}_T - \boldsymbol{r}_{R_i}\right)^T\left(\boldsymbol{r}_T - \boldsymbol{r}_{R_i}\right)\right]^{3/2}} \tag{71}$$

Our next derivative of S_i will be with respect to $\boldsymbol{v}_T$

$$\frac{dS_i}{d\boldsymbol{v}_T} = \frac{\left(\boldsymbol{r}_T - \boldsymbol{r}_{R_i}\right)^T}{\left[\left(\boldsymbol{r}_T - \boldsymbol{r}_{R_i}\right)^T\left(\boldsymbol{r}_T - \boldsymbol{r}_{R_i}\right)\right]^{1/2}} \tag{72}$$

Our last derivative of S_i is with respect to f_T

$$\frac{dS_i}{df_T} = -c\frac{f_i}{f_T^2} \tag{72}$$

We can utilize this method to determine which specific geometries will provide degenerate solutions. Some of these degenerate geometries are enumerated in the following paragraphs. However, we can also show that the solution will be locally unique for a transmitter having a general position and velocity. For example, consider the general geometry show in Tables 11 and 12. Using this configuration to calculate our observable for each receiver and substituting these results into the Jacobi matrix, we find that the condition number is about 2×10^4. This tells us that although the general case is not degenerate. It also tells us that some geometries may lead to a poorly conditioned Jacobi matrix, suggesting a large sensitivity to measurement noise.

Table 11. Position, velocity, and carrier frequency of the transmitter for the general geometry example

Transmitter						
Position (km)			Velocity (km/s)			Frequency (Hz)
8000	6000	0	0	5	5	1×10^9

Table 12. Position and velocity of each receiver for the general geometry example

Receivers						
Receiver	Position (km)			Velocity (km/s)		
1	1319	10	169	4.9	17.4	2.7
2	8138	2628	612	0.25	7.9	0.57
3	5310	-6359	-267	8	1.3	0.82
4	11264	-7437	554	4.3	3.6	0.24
5	42390	-104890	930	1.9	0.33	0.03
6	-5032	-11865	334	4.9	-2.7	0.11
7	4997	-4716	-190	6.4	4.5	0.45

Our first degenerate geometry is the “string of pearls” geometry where all satellites, including all receivers and transmitters, are in a leader-follower formation in the same circular orbit. An example of this geometry can be seen in Figure 30. In this formation, the relative velocity between each of the receivers and the transmitter will be zero. Looking at the Jacobi matrix we can see that this will reduce the rank from seven to three.

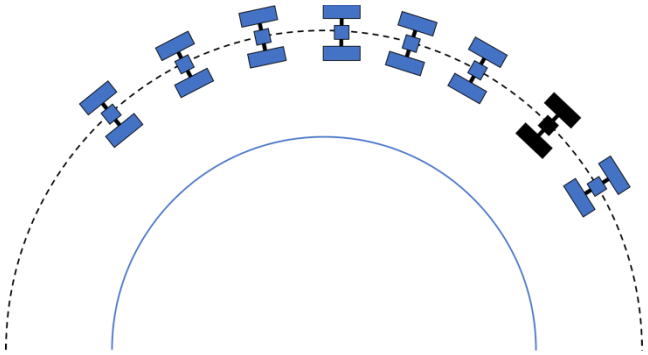

Figure 30. An example of the "string of pearls" geometry

The next degenerate geometry that we will look at is where all receivers and the transmitter are lined up along a single line of sight. An example of this geometry can be seen in Figure 31.

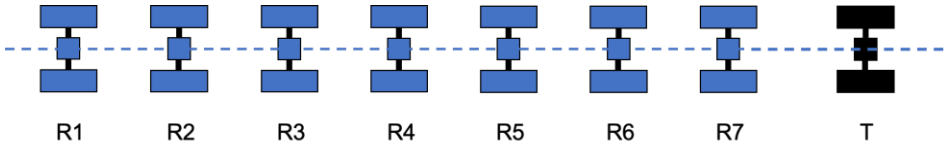

Figure 31. An example of the geometry where each receiver has the same line of sight to the transmitter

We can prove that this geometry is degenerate by looking at the Jacobi matrix. For this geometry, Eq. 72 would be the same for each of the receivers. Thus, the Jacobi matrix would have a rank of five rather than seven. This geometry is very rare because the measurements from each receiver must be taken when the receivers line up.

4.3.3 IOD from Non-Concurrent Frequency Measurements

For the single receiver taking FOA measurements over time case. We can now set up our system of nonlinear equations of the form $S(\boldsymbol{x}) = 0$. We will define S to be

$$S = \begin{matrix} \left(\frac{f_R(t_1) - f_T}{f_T}\right) = -\left(\boldsymbol{v}_T(t_1) - \boldsymbol{v}_R(t_1)\right)^T \frac{\boldsymbol{r}_T(t_1) - \boldsymbol{r}_R(t_1)}{\|\boldsymbol{r}_T(t_1) - \boldsymbol{r}_R(t_1)\|} \\ \vdots \\ \left(\frac{f_R(t_k) - f_T}{f_T}\right) = -\left(\boldsymbol{v}_T(t_k) - \boldsymbol{v}_R(t_k)\right)^T \frac{\boldsymbol{r}_T(t_k) - \boldsymbol{r}_R(t_k)}{\|\boldsymbol{r}_T(t_k) - \boldsymbol{r}_R(t_k)\|} \end{matrix} \tag{73}$$

The knowns in our system include the position and velocity of the receiver at each measurement time and the time at each measurement, t_i. The observables include the frequency measured by the receiver at each measurement time. The unknowns include the position and velocity of the transmitter at each measurement time and the carrier frequency. We assume that the carrier frequency is constant over time. Our observables are related to knowns and unknowns using Eq. 63.

To reduce the number of unknowns, we relate the position and velocity of the transmitter at each measurement to the position and velocity of the transmitter at the first measurement. As long as we know the time elapsed between measurements we can us Kepler's equation to accomplish this task.

At the moment, we have only attempted to solve the non-concurrent frequency-based IOD problem using the Newton-Raphson method. The Newton-Raphson method is an iterative, gradient-based algorithm used to solve nonlinear system of equations [47]. The algorithm requires an initial guess, and a reasonable guess at that. As discussed later in this section, an unreasonable guess may cause the method to not converge or converge to an incorrect solution. Our solver uses the initial guess to calculate the Jacobi matrix using forward finite differencing. The step is then calculated by dividing the residual from the initial guess by the Jacobi matrix. This step is then subtracted from the current guess to form a new guess. We then calculate the error by taking the norm of the residual from the new guess. We repeat these steps with the new guess until the error reaches a certain threshold.

We developed a general case to test this method. Tables 13 and 14 provide the orbital states of the transmitter and receiver at the time of the initial measurement, respectively.

Table 13. Position, velocity, and carrier frequency of the transmitter at the time of the first measurement for the general geometry example

Position (km)			Velocity (km/s)		
36515	21082	0	-1.537	2.627	0

Table 14. Position and velocity of the receiver at the time of the first measurement for the general geometry example

Receiver					
Position (km)			Velocity (km/s)		
10629	15133	68161	-4.017	3.072	0.408

Our initial findings show that the Newton-Raphson method would converge if the initial guess of the position was within 100 km and the velocity was within 100 m/s. We have also found instances outside of the regions discussed above where the method converges to an incorrect orbit. This tells us that although the problem is locally unique, it is not globally unique.

4.3.4 Relative IOD from Non-Concurrent Frequency Measurements

In the special case where both the transmitter and receiver are in orbit, the situation may arise when the two are known to be close to one another. In such a case, it is often reasonable for IOD purposes to assume the relative motion between the transmitter and receiver is governed by the so-called Clohessy-Wiltshire (CW) equations. Under this assumption, we linearize the dynamics and analytically compute the state transition matrix---thus allowing us to propagate a relative state forwards (or backwards) in time with a simple linear transformation. That is, if $\boldsymbol{r}$ is the

relative position and $\boldsymbol{v}$ is the relative velocity, we may propagate the relative translational state from time t_0 to time t according to

$$\boldsymbol{x}(t) = \begin{bmatrix} \boldsymbol{r}(t) \\ \boldsymbol{v}(t) \end{bmatrix} = \begin{bmatrix} \boldsymbol{\Phi_{rr}} & \boldsymbol{\Phi_{rv}} \\ \boldsymbol{\Phi_{vr}} & \boldsymbol{\Phi_{vv}} \end{bmatrix} \begin{bmatrix} \boldsymbol{r}(t_0) \\ \boldsymbol{v}(t_0) \end{bmatrix} = \begin{bmatrix} \boldsymbol{\Phi_r} \\ \boldsymbol{\Phi_v} \end{bmatrix} \boldsymbol{x}(t_0) \tag{74}$$

Now, we may apply this to the Doppler equation as shown in Eq. 63 to find the frequency observed by the receiver at time t,

$$f(t) = \left(1 - \frac{\boldsymbol{v}(t)^T \boldsymbol{u}(t)}{c}\right) f_T \tag{75}$$

Recognizing that $\boldsymbol{u}(t) = \boldsymbol{r}(t)/\|\boldsymbol{r}(t)\|$, we find that

$$cf(t) = cf_T - f_T \frac{\boldsymbol{v}(t)^T \boldsymbol{r}(t)}{\|\boldsymbol{r}(t)\|} \tag{76}$$

which we may rewrite in terms of the state at t_0, $\boldsymbol{x}_0 = \boldsymbol{x}(t_0)$

$$cf(t) = cf_T - f_T \frac{\boldsymbol{x}_0^T \boldsymbol{\Phi}_{\boldsymbol{v}}^T \boldsymbol{\Phi}_{\boldsymbol{r}} \boldsymbol{x}_0}{(\boldsymbol{x}_0^T \boldsymbol{\Phi}_{\boldsymbol{r}}^T \boldsymbol{\Phi}_{\boldsymbol{r}} \boldsymbol{x}_0)^{1/2}} \tag{77}$$

Preliminary numerical experimentation has shown this seven-parameter estimation problem (unknowns of 3D position, 3D velocity, and 1D transmit frequency) to be fully observable for a transmitter and receiver in general orbits. There do exist degenerate configurations, such as those discussed in prior sections (e.g., the Doppler shift will always be zero for any trailing orbit because the range-rate is zero).

4.4 Extended Kalman Filter (EKF) with MUSIC Measurements

We implemented a proof-of-concept EKF to demonstrate the performance of angles-only IOD using RF-based DOA measurements obtained via the MUSIC algorithm. Details of the MUSIC algorithm are in Section 3.1 and EKF background is discussed in Section 3.4. This example assumes a transmitter broadcasting at a frequency of 27 GHz (example Ka band signal). We

assume this signal is detected by a receiver having a uniform rectangular array (URA) with elements in a 13x13 grid pattern. The MUSIC algorithm is used to construct DOA measurements once every three minutes (i.e., a MUSIC measurement is supplied to EKF every three minutes).

Now, consider the situation where the transmitter and receiver are on different orbits. For the sake of demonstrating efficacy, we choose arbitrary (but realistic) orbital elements for each, as summarized in Table 15.

Table 15. Initial conditions for transmitter and receiver for EKF demonstration with MUSIC

Spacecraft	Semi-Major Axis (km)	Eccentricity (~)	Inclination (deg)	RAAN (deg)	Argument of Perigee (deg)	True Anomaly (deg)
Transmitter	8091.8	0.10	39	221	30	15
Receiver	8091.8	0.15	40	220	30	15

Finally, assuming a signal-to-noise ratio (SNR) of 2 dB for the transmitter, we may look at the EKF state estimation performance over a period of three orbits (about 6 hours). These results are shown in Figure 32 and Figure 33, with the thick black line showing the state estimation error, and the red/blue lines showing the covariance bounds.

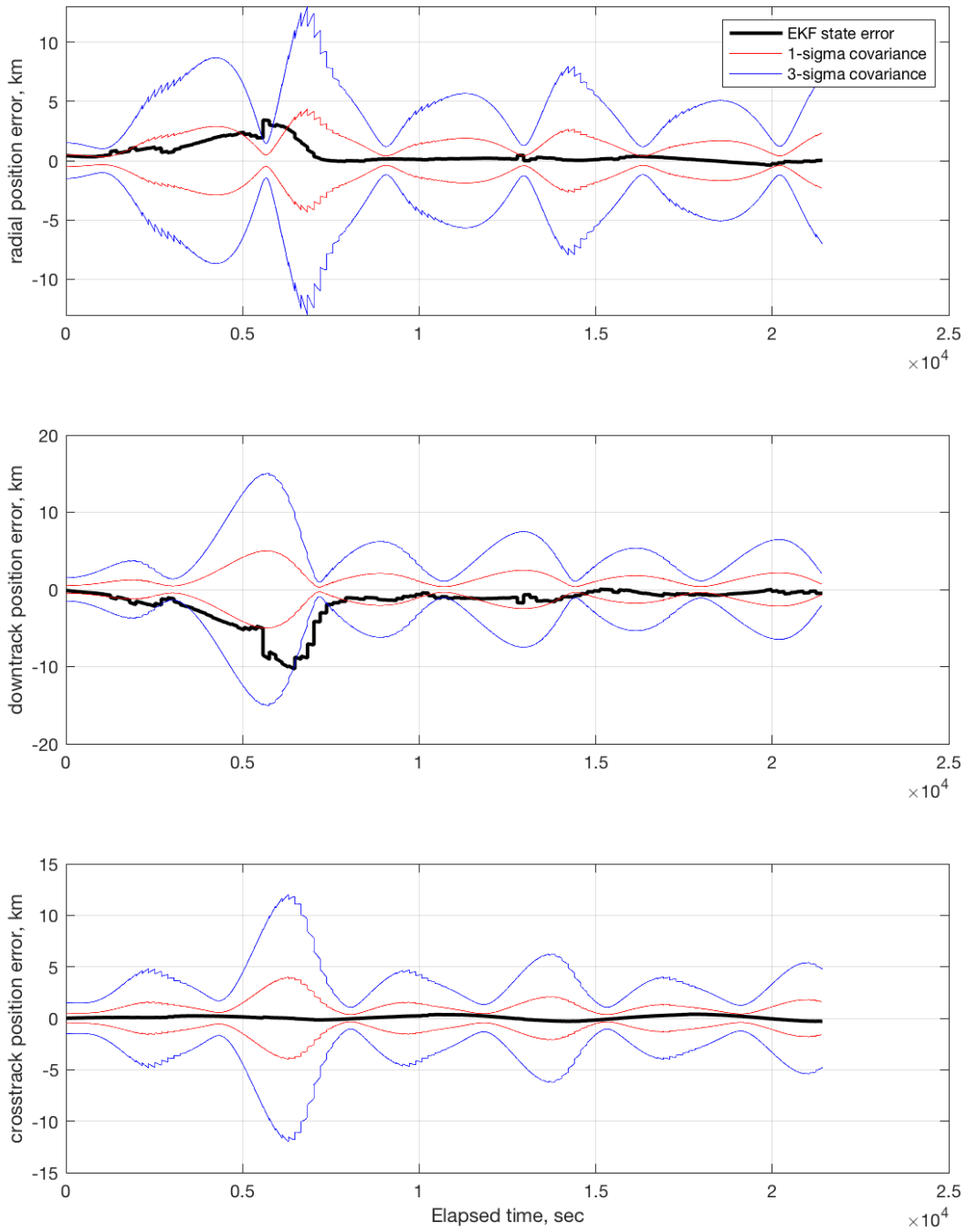

Figure 32. EKF position estimation performance over three orbits

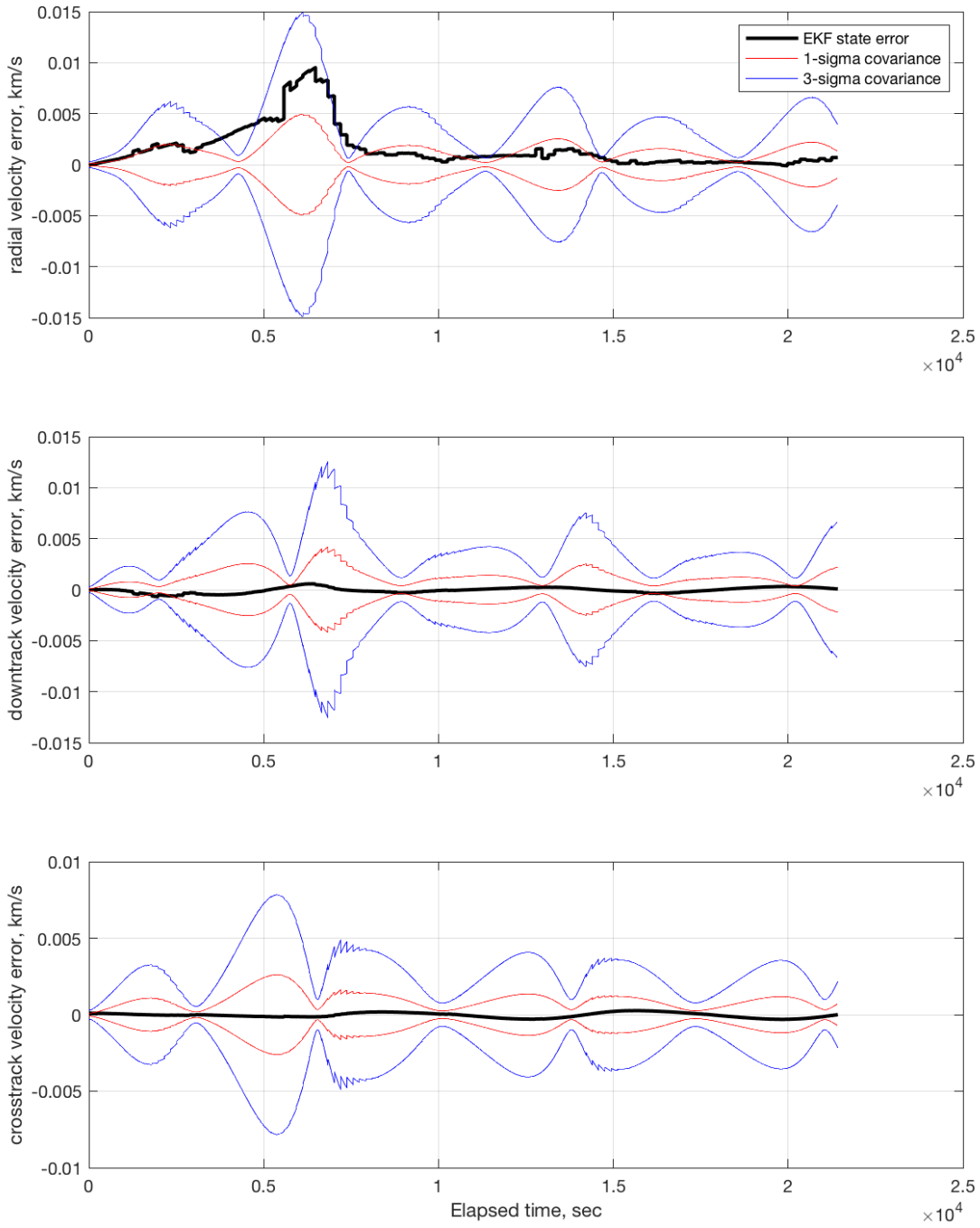

Figure 33. EKF velocity estimation performance over three orbits

5 CONCLUSIONS

Radio frequency (RF) signals from an unknown transmitter may be used to infer the position and velocity of the transmitter. This may be accomplished using a number of different RF observables, including: direction-of-arrival (DOA), time difference of arrival (TODA), and Doppler shift. In this work, we investigated the efficacy of all three of these RF observables for transmitter localization.

The work on this grant began by studying the various algorithms and techniques to extract state data from RF observables. We explored the MUltiple SIgnal Classification (MUSIC) algorithm for DOA measurements, classic TDOA measurements, and a variety of Doppler measurements. The Doppler measurements included a simple frequency shift, but also included more complicated measurements types like frequency difference on arrival (FDOA) and frequency ratio on arrival (FROA).

The various measurement types were evaluated for a few different types of transmitter localization. The first was the geolocation problem, where our objective was to determine the location of a stationary transmitter on the surface of Earth. Next, we considered determination of the full orbital state (position and velocity) for a transmitter in Earth orbit. In this case we studied both the initial orbit determination (IOD) and precise orbit determination (POD) problems. For the IOD problem, a solution was developed for the special case of concurrent measurements---though this requires at least seven receivers in general position. We began the study of a solution procedure for non-concurrent measurements, though more work remains to be done to arrive at an algorithm that works when no a priori state knowledge. For the POD problem, we studied the efficacy of the MUSIC algorithm within an extended Kalman filter (EKF) estimation framework.

Our preliminary analysis suggests that RF-based observables may be used for determining the state of an unknown transmitter. Further work is required to have stable and globally convergent algorithms for solving this problem in practice.

6 BIBLIOGRAPHY

[1] M. Kayton and W. Fried, Avionics Navigation Systems, 2nd Ed, Wiley, 1997.

[2] B. Tan, K. Woodbridge and K. Chetty, "Areal-time high resolution passive wifi Doppler-radar and its applicaitons," in *2014 International Radar Conference*, 2014.

[3] S. Ziraril, P. Canalda and F. Spies, "Wifi GPS Based Combined Positioning Algorithm," in *2010 IEEE International Conference on Wireless Communications, Networking and Information Security (WCNIS)*, 2010.

[4] G. Opshaug, J. Do and D. Rubin, "Doppler-aided positioning, navigation, and timing using broadcast television signals". USA Patent 8,125,389, 2012.

[5] H. Sun, D. Tan, Y. Lu and M. Lesturgie, "Applications of Passive Surveillance Radar Systems using Cell Phojne Base Station Illuminators," *IEEE Aerosapce and Electronic Systems Magazine,* **vol. 25**, no. 3, pp. 10-18, 2010.

[6] J. Ashjaee, "GPS Doppler Processing for Precise Positioning in Dynamics Applicaionts," *Navigation,* **vol. 25**, no. 3, pp. 370-385, 1985.

[7] S. Wu and V. Ondrasik, "Orbit Determination of Low-Altitude Earth Satellites using GPS RF Doppler," in *PLANS '82*, 1982.

[8] E. P. Krider, R. C. Noggle, A. E. Pifer and D. L. Vance, "Lightning direction-finding systems for forest fire detection," *Bulletin of the American Meteorological Society,* **vol. 61**, p. 980–986, 1980.

[9] J. Kennedy and M. C. Sullivan, "Direction finding and ``smart antennas" using software radio architectures," *IEEE Communications Magazine,* **vol. 33**, p. 62–68, 1995.

[10] B. Hofmann-Wellenhof, H. Lichtenegger and J. Collins, Global positioning system: theory and practice, Springer Science & Business Media, 2012.

[11] S. Shuster, A. J. Sinclair and T. A. Lovell, "Initial relative-orbit determination using heterogeneous TDOA," in *2017 IEEE Aerospace Conference*, 2017.

[12] W. H. Guier and G. C. Weiffenbach, "A satellite Doppler navigation system," *Proceedings of the IRE,* **vol. 48**, p. 507–516, 1960.

[13] X. Ning and J. Fang, "Spacecraft autonomous navigation using unscented particle filter-based celestial/Doppler information fusion," *Measurement Science and Technology,* **vol. 19**, p. 095203, 2008.

[14] K. C. Ho and Y. T. Chan, "Solution and performance analysis of geolocation by TDOA," *IEEE Transactions on Aerospace and Electronic Systems,* **vol. 29,** p. 1311–1322, 1993.

[15] L. I. Jinzhou, G. U. O. Fucheng and W. Jiang, "A linear-correction least-squares approach for geolocation using FDOA measurements only," *Chinese Journal of Aeronautics,* **vol. 25**, p. 709–714, 2012.

[16] K. Ho and Y. T. Chan, "Geolocation of a known altitude object from TDOA and FDOA measurements," *IEEE transactions on aerospace and electronic systems,* **vol. 33**, p. 770–783, 1997.

[17] T. T. J. Brooks, H. H. C. Bakker, K. A. Mercer and W. H. Page, "A review of position tracking methods," in *1st International conference on sensing technology*, 2005.

[18] R. Schmidt, "Multiple emitter location and signal parameter estimation," *IEEE transactions on antennas and propagation,* **vol. 34**, p. 276–280, 1986.

[19] M. Jalali, M. N. Moghaddasi and A. Habibzadeh, "Comparing accuracy for ML, MUSIC, ROOT-MUSIC and spatially smoothed algorithms for 2 users," in *2009 Mediterrannean Microwave Symposium (MMS)*, 2009.

[20] Z. H. U. Liang, G. O. N. G. Wen-fei and G. U. O. Xu-qiang, "Research on GNSS System Single Interference Direction Finding," *DEStech Transactions on Computer Science and Engineering,* 2019.

[21] H. Wang, Q. Chang, Y. Xu and X. Li, "Estimation of Interference Arrival Direction Based on a Novel Space-Time Conversion MUSIC Algorithm for GNSS Receivers," *Sensors,* **vol**. **19**, p. 2570, 2019.

[22] P. Gupta and S. P. Kar, "MUSIC and improved MUSIC algorithm to estimate direction of arrival," in *2015 International Conference on Communications and Signal Processing (ICCSP)*, 2015.

[23] C. R. Dongarsane and A. N. Jadhav, "Simulation study on DOA estimation using MUSIC algorithm," *International Journal of Technology And Engineering System (IJTES),* **vol. 2**, p. 54–57, 2011.

[24] A. Vesa, "Direction of arrival estimation using MUSIC and root–MUSIC algorithm," in *18th Telecommunications Forum, Pg*, 2010.

[25] C. Wen, Z. Wen, M. Lina, W. Yanqun, W. Jun and H. Zhengliang, "A MUSIC based Interference Suppression Algorithm and Its Application in weak Target Tracking," in *2019 IEEE 2nd International Conference on Information Communication and Signal Processing (ICICSP)*, 2019.

[26] S. Shao, A. Liu, C. Yu, H. Yang, Y. Li and B. Li, "Spatial time-frequency distribution of cross term-based direction-of-arrival estimation for weak non-stationary signal," *EURASIP Journal on Wireless Communications and Networking,* **vol. 2019**, p. 1–12, 2019.

[27] L. Qiu, T. Lan and Y. Wang, "A Sparse Perspective for Direction-of-Arrival Estimation Under Strong Near-Field Interference Environment," *Sensors,* **vol. 20**, p. 163, 2020.

[28] P. Misra and P. Enge, Global positioning system: signals, measurements, and performance, Ganga-Jamuna Press, 2006.

[29] J. Saastamoinen, "Atmospheric correction for the troposphere and stratosphere in radio ranging satellites," *The use of artificial satellites for geodesy,* **vol. 15**, p. 247–251, 1972.

[30] H. S. Hopfield, "Two-quartic tropospheric refractivity profile for correcting satellite data," *Journal of Geophysical research,* **vol. 74,** p. 4487–4499, 1969.

[31] M. C. Kelley, The Earth's ionosphere: plasma physics and electrodynamics, **vol. 96**, Academic press, 2009.

[32] J. A. Klobuchar, "Ionospheric time-delay algorithm for single-frequency GPS users," *IEEE Transactions on aerospace and electronic systems,* p. 325–331, 1987.

[33] A. J. Sinclair, T. A. Lovell and J. Darling, "RF localization solution using heterogeneous TDOA," in *2015 IEEE Aerospace Conference*, 2015.

[34] S. W. Asmar, J. W. Armstrong, L. Iess and P. Tortora, "Spacecraft Doppler tracking: Noise budget and accuracy achievable in precision radio science observations," *Radio Science,* **vol. 40**, 2005.

[35] A. Einstein, "On the electrodynamics of moving bodies," *Annalen der Physik,* **vol. 17**, p. 50, 1905.

[36] J. A. Christian, "StarNAV: Autonomous Optical Navigation of a Spacecraft by the Relativistic Perturbation of Starlight," *Sensors,* **vol. 19**, p. 4064, 2019.

[37] J. A. Klobuchar, "Ionospheric effects on Earth-space propagation," 1983.

[38] H. S. Hopfield, "The effect of tropospheric refraction on the Doppler shift of a satellite signal," *Journal of Geophysical Research,* **vol. 68**, p. 5157–5168, 1963.

[39] A. Gelb, Applied Optimal Estimation, MIT Press, 1974.

[40] P. Maybank, Stochastic Models: Estimation and Control, **Vol. 2,** Academic Press, 1982.

[41] R. Brown and P. Hwang, Introduction to Random Signals and Applied Kalman Filtering, Wiley, 1997.

[42] B. Tapley, B. Schutz and G. Born, Statistical Orbit Determination, Elsevier, 2004.

[43] J. Crassidis and J. Junkins, Optical Estimation of Dynamic Systems, Chapman & Hall/CRC, 2004.

[44] J. Carpenter and C. D'Souza, *Navigation Filter Best Practices, NASA/TP-2018-219822,* NASA, 2018.

[45] J. Nash, "The imbedding problem for Riemannian manifolds," *Annals of mathematics,* p. 20–63, 1956.

[46] J. Moser, "A rapidly convergent iteration method and non-linear partial differential equations-I," *Annali della Scuola Normale Superiore di Pisa-Classe di Scienze,* **vol. 20**, p. 265–315, 1966.

[47] T. J. Ypma, "Historical development of the Newton–Raphson method," *SIAM review,* **vol**. **37**, p. 531–551, 1995.

LIST OF ACRONYMS, ABBREVIATIONS, AND SYMBOLS

Acronym/ Abbreviation	Description
AFRL	Air Force Research Laboratory
DOA	Direction of Arrival
EKF	Extended Kalman Filter
FDOA	Frequency Difference on Arrival
FROA	Frequency Ratio on Arrival
IOD	Initial Orbit Determination
MUSIC	MUltiple SIgnal Classification
RF	Radio Frequency
RPI	Rensselaer Polytechnic Institute
SNR	Signal-to-Noise Ratio
TDOA	Time Difference of Arrival

DISTRIBUTION LIST

DTIC/OCP
8725 John J. Kingman Rd, Suite
0944 Ft Belvoir, VA 22060-6218 1 cy

AFRL/RVIL
Kirtland AFB, NM 87117-5776 1 cy

Official Record Copy
AFRL/RVS/Thomas Lovell 1 cy